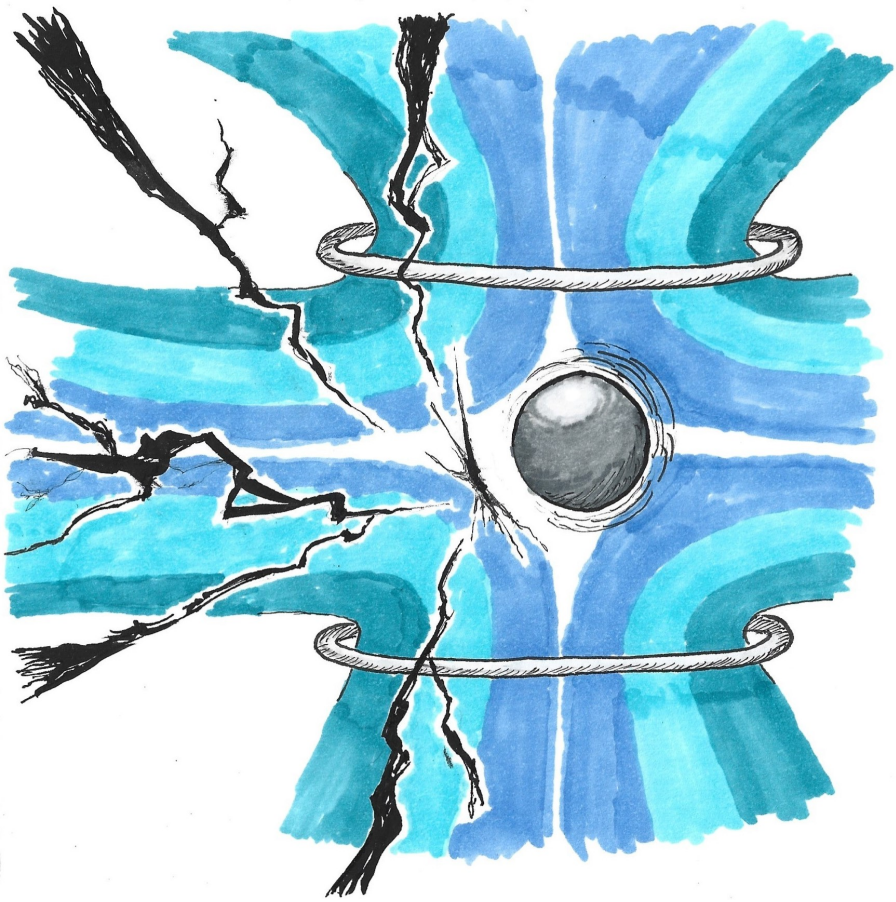

Detection of Scalar Wave Dark Matter with a Levitated Superconductor

Master's thesis in Physics

IOANNIS MOUTSIS

DEPARTMENT OF PHYSICS

CHALMERS UNIVERSITY OF TECHNOLOGY
Gothenburg, Sweden 2025
www.chalmers.se

Master's thesis 2025

Detection of Scalar Wave Dark Matter with a Levitated Superconductor

IOANNIS MOUTSIS

CHALMERS
UNIVERSITY OF TECHNOLOGY

Department of Physics
Division of Subatomic, High Energy and Plasma Physics
Theoretical Subatomic Physics Group
Chalmers University of Technology
Gothenburg, Sweden 2025

Detection of Scalar Wave Dark Matter with a Levitated Superconductor.

IOANNIS MOUTSIS

© IOANNIS MOUTSIS, 2025.

Supervisor: Riccardo Catena, Physics
Examiner: Riccardo Catena, Physics

Master's Thesis 2025
Department of Physics
Division of Subatomic, High Energy and Plasma Physics
Theoretical Subatomic Physics Group
Chalmers University of Technology
SE-412 96 Gothenburg
Telephone +46 31 772 1000

Cover: Dark Matter hits the levitated superconductor, Ioannis Moutsis, ink on paper and color with alcohol markers, 2025

Typeset in LaTeX
Printed by Chalmers Reproservice
Gothenburg, Sweden 2025

Detection of Scalar Wave Dark Matter with a Levitated Superconductor
IOANNIS MOUTSIS
Physics Department
Chalmers University of Technology

Abstract

The nature of dark matter is one of the most elusive problems in modern physics. With varying candidates and a vast range of possible particle masses, there is still no direct evidence of dark matter through an experimental observation. In this thesis, the possibility of detecting dark matter in a laboratory setup is theoretically investigated. The candidate in question will be the scalar case of the wave-like dark matter, a particle dark matter that belongs in the ultralight mass spectrum. The proposal is that this type of dark matter can be described by a classical wave instead of a quantum field and will interact with neutrons in matter through a simple, linear, non-derivative term in the Lagrangian. This interaction would result in an sinusoidal force that can be detected in a proposed magnetically levitated superconductor experiment. The experimental setup is parametrized as a coupled harmonic oscillator system, where a vibrational shield is installed to minimize vibrational noise. Through stochastic modeling of vibrational noise and numerical methods such as Monte Carlo simulations, the motion of the target superconductor is studied. The end result of this analysis is the projected sensitivity of the proposed experiment, expressed as exclusion limits on the coupling strength as a function of dark matter mass. We conclude that in a two-stage model, with experimental parameters corresponding to a possible levitation experiment in Chalmers, the vibrational noise is identified as the dominant noise source, exceeding both thermal, imprecision and back-action noise due to the measurement device (SQUID), significantly limiting the sensitivity. For comparison, the minimum coupling per unit mass in an ideal case with linearly scaled down vibrational noise is also presented, along with an analytical sensitivity projection.

Keywords: wave dark matter, dark matter, maglev, levitated superconductor, scalar coupling, direct detection, Monte Carlo.

Acknowledgements

I would like to express my gratitude to many people.

To my supervisor, Professor Riccardo Catena, for giving me the opportunity to work in theoretical physics and for his unwavering support. To Professor Witlef Wieczorek and Fabian Resare, for their invaluable insight and many discussions about the experiment behind the theory.

To my family, my mother and father, for their continuous support and for giving me the means to pursue this challenging field of study.

To you, my beloved Sofia, for being a hopeful sunshine amid the clouds of Sweden.

Ioannis Moutsis, Gothenburg, June 2025

List of Acronyms

Below is the list of acronyms that have been used throughout this thesis listed in alphabetical order:

DE	Differential Equation
DM	Dark Matter
EP	Equivalency Principle
MC2	Department of Microtechnology and Nanoscience at Chalmers
NPS	Noise Power Spectrum
PSD	Power Spectral Density
QM	Quantum Mechanics
QFT	Quantum Field Theory
QTL	Quantum Technologies Lab
SQL	Standard Quantum Limit
SNR	Signal to Noise Ratio
SQUID	Superconducting Quantum Interference Device
WDM	Wave Dark Matter
WEP	Weak Equivalency Principle

Contents

1
Introduction

Dark matter needs no introduction. It famously stands as one of the most puzzling unsolved mysteries in physics today: a grand part of matter in the universe that cannot be *seen*. In this chapter we shall briefly discuss the history of the dark matter physics and some of most prolific candidates that are being investigated today, along with the main focus of this thesis: a kind of dark matter that can be described as a classical wave.

1.1 Dark Matter

The historical development of the notion of dark matter begins in the 1930's with the investigation of galaxy clusters by Fritz Zwicky. Zwicky's analysis of the Coma Cluster revealed an unexpectedly high velocity dispersion among the constituent galaxies. [1]. By applying the *virial theorem*[1] and assuming an average galactic mass of $10^9 M^{\odot}$ (as estimated by Edwin Hubble), Zwicky expected a velocity dispersion of roughly 80 km/s for the system. Instead, he observed dispersions near 1000 km/s, exceeding expectation by a vast amount.

This discrepancy suggested that the total gravitational mass of the cluster was vastly greater than the luminous matter (i.e. the matter that could be *seen*) could account for. This other, unseen type of matter was dubbed "dunkle Materie" (trans. dark matter). Zwicky's subsequent refinement of the cluster's parameters led him to derive a mass-to-light ratio of approximately 500 solar units, although modern recalibrations using updated Hubble constant values have reduced this by roughly a factor of eight [7]. Around the same time, Sinclair Smith [8] conducted similar studies on the Virgo Cluster, reaching comparable conclusions. In any case, according to the observations the majority of mass in the clusters is invisible.

Other findings hinting to the existence of such a different kind of matter came from the study of galactic rotation curves. A galaxy's rotation curve plots the orbital velocity of stars and gas as a function of their distance from the galactic center[9]. In classical Newtonian systems we expect the orbital speed of objects to decline with increasing distance from the central mass (a Keplerian profile). This can be observed in our Solar system, where in the edge of it the velocity of bodies is $v \propto 1/\sqrt{r}$, with r being the distance from the Sun. However, optical spectroscopy

[1] The well known virial theorem relates the kinetic energy and gravitational potential of a system by $\langle T \rangle = -\langle U \rangle/2$, but it can be argued that it cannot be applied if the cluster is unstable.

observations of luminous spiral galaxies [10] consistently revealed deviations from this expectation. Rather than falling off, rotation curves flatten at large radii, indicating that mass continues to increase with distance from the center. These findings were soon corroborated and extended by radio observations, particularly those using the 21-cm hydrogen line [11], which allowed astronomers to trace the rotation of neutral hydrogen gas in the outermost parts of galaxies, well beyond the region populated by visible stars. The rotational velocity is approximately constant in this outer invisible area encompassing a galaxy, which is named the *dark matter halo*.

Another method of probing the dark matter distribution in galaxies emerged in the 1970's, called *gravitational lensing*. According to General Relativity gravitational lensing occurs when massive objects curve spacetime and deflect the path of light passing near them, meaning that by observing distortions in the images of background galaxies the distribution of otherwise invisible matter can be inferred. The first confirmed case of gravitational lensing was reported in 1979 by Walsh, Carswell, and Weymann [13], who observed two nearly identical quasar images separated by 5.6 arcseconds, suggesting they were two lensed images of the same object. Later observations by Lynds and Petrosian in 1988 [14] further confirmed this effect by observing partial "Einstein-rings" in galaxy clusters. For example, calculations [15] showed that the mass-to-light ratio in the Abell 370 cluster must be about $10^2 - 10^3$ solar units, a similar magnitude to the original velocity dispersion observations.

1.2 Candidates

The convergence of the first independent lines of observations provided compelling support for the dark matter hypothesis. Research then quickly moved from acknowledging the existence of dark matter to attempting describing its nature and understanding its composition. Over the decades many kinds of matter have been proposed to be a promising candidate for comprising a large percentage, if not the whole, of dark matter.

A key distinction between different candidates lies to wether or not they are moving with velocities close to the speed of light. Particles moving with relativistic velocities compose the *hot dark matter*, while particles moving with much lower, non-relativistic, velocities compose the *cold dark matter*. Simulations show that if dark matter were hot, large structures such as galaxy clusters would form first and later fragment into smaller ones. In contrast, cold dark matter would clump into smaller halos first, which would later merge to form larger structures. Deep-field observational evidence [16] supports the later scenario, where galaxies are formed first, followed by the formation of clusters and superclusters, therefore ruling that most dark matter is cold.

Another important classification between candidates is wether they are created *thermally* or *non-thermally*. Thermal dark matter particles were in equilibrium with the primordial plasma and "froze out" as the Universe expanded and cooled. This mechanism predicts a specific relationship between the particle's interaction strength and

the relic abundance observed today. On the other hand, non-thermal dark matter was never in thermal equilibrium either because it was produced too late or interacted too weakly with the thermal bath. Importantly, this allows light particles to be cold and stable, as long as their production mechanism avoids relativistic behavior during structure formation.

1.2.1 Baryonic Dark Matter

The very first and probably obvious solution to the dark matter problem is that it is comprised of regular baryonic matter that is faintly luminous for some reason, e.g. cold gases or compact objects like brown dwarfs, neutron star or black holes (collectively referred to as *MACHOs*). Gravitational microlensing surveys, such as those conducted by the EROS-2 Collaboration [17], have shown that MACHOs constitute a small fraction (less than 8%) of the matter needed to explain halos. Additionally, precise measurements of the cosmic microwave background (CMB) and Big Bang nucleosynthesis, particularly from the Planck satellite, have constrained the baryon density of the Universe to only about 7% of the total matter content. Thus, the baryonic hypothesis has been effectively ruled out.

1.2.2 Neutrinos

Among the earliest proposed candidates were the Standard Model neutrinos. Their longevity and lack of electromagnetic or strong interactions made them promising on paper. However, due to their low mass and thermal origin, these particles were highly relativistic in the early Universe. Thus, neutrinos falling in the hot dark matter category means that they cannot realistically be the dominant dark matter component. While relic neutrinos still exist and contribute marginally to the total matter content, they fall far short of explaining the full dark matter abundance.

1.2.3 WIMPs

Perhaps the most extensively studied dark matter candidates are the *Weakly Interacting Massive Particles* (WIMPs). With masses typically in the GeV–TeV range, WIMPs naturally arise in several beyond-the-Standard-Model theories, including *supersymmetry*. WIMPs could have been thermally produced in the Early Universe and at a later time (as temperatures would drop below their mass scale) decouple from the thermal plasma. The relic density produced with this mechanism coincides with the current measurements of dark matter density. This coincidence along with the fact that WIMPs can confirm other exciting particle physics theories is often referred to as the *WIMP miracle* [18].

The theoretical miracle though is not reaching the detection front. Several decades of experimental searches, both direct and indirect, have yet to yield any definitive signals. This lack of evidence has led to tighter constraints on their properties and has pushed viable WIMP parameter space into increasingly higher masses and lower interaction cross-sections.

1.3 Wave-like Dark Matter

One of the main classes of dark matter candidates is the field-like particles, where the main characteristic is the ultra light mass associated with the field of the particle. This candidate is the singular focus of this thesis and would be refer to as *Wave Dark Matter* (WDM) for reasons to be explained shortly.

Dynamical measurements appear to suggest that the local energy density of dark matter is around $\rho_{DM} \approx (0.04 \text{ eV})^2 = 0.3 \text{ GeV cm}^{-3}$ [19] and even up to 0.49 GeV cm^{-3} [20]. From quantum theory, every particle has a *De Broglie wavelength* associated with it

$$\lambda_{\text{dB}} = \frac{2\pi}{p}, \tag{1.1}$$

where p is the momentum of the particle. The wavelength λ_{dB} defines a phase space, in whose respective volume a certain number of particles is confined. This particle number can be written in terms of mass density as

$$N_{\text{dB}} = \frac{\lambda_{\text{dB}}^3 \, \rho_{\text{DM}}}{m}. \tag{1.2}$$

If the phase space density will be high enough, then the average inter-particle separation will be much lower than the average de Broglie wavelength, meaning that the particle nature would be much closer to that of a wave instead of a particle. Another way to think of this is by observing that in quantum field theory, the particles are in fact excitations of fields, and for either bosonic or fermionic field, the quantum fluctuations of the number of particles in a confined volume is inversely proportional to the particle number, meaning that a very high particle number, resulting from a very low mass in Eq. (1.2), implies negligible quantum fluctuations (for a more detailed calculation of this statement, see Appendix A).

In essence, the fact that this specific dark matter candidate has such a low mass, means that its field can be effectively approximated as a *classical field* or a *classical wave*. One could compare this to the treatment of light in quantum theory and in classical electromagnetism, however it is important to note that while the mass of light is exactly zero, WDM candidates are still dark matter candidates and must have non zero mass to interact gravitationally with matter, thus the wave treatment of dark matter will always be an approximate solution.

While the nature of boundaries in the quantum and classical world is a fascinating topic with many unanswered questions, in our case we shall assume that, in general, masses well below 30 eV are considered to be in the WDM area. However, as already mentioned, we cannot assume the mass to be arbitrarily low. A lower bound can be defined by the maximum de Broglie wavelength size allowed by astronomical observations, such as the size of dwarf galaxies [21], which is about $m \leq 10^{-22}$. Masses near that lower bound, $10^{-22} - 10^{-20}$ eV, constitute the so called *fuzzy dark matter*. While going even lower than fuzzy cold dark matter is allowed, the particle number of the specific candidate has to be a fraction of the total dark matter

observed and at an extremely low scale the candidate would begin to resemble dark energy more than dark matter ($\approx 10^{-33}$ eV).

1.3.1 Axions and ALPs

One of the most searched for and thoroughly studied wave dark matter candidate is the QCD *axion*, which is a pseudo-Nambu-Goldstone boson. The axion is currently part of a proposed Standard Model extension and besides being a good pseudo-scalar WDM candidate, it offers solutions to other problems, such as the *strong CP problem* [22].

CP-Symmetry is known to be violated in weak interactions but for unknown theoretical reasons such violation is still unobserved in strong interactions. This means that, in the QCD lagrangian, CP-violating terms (known as θ-terms) seem to be canceled out. The most popular solution, the *Peccei–Quinn mechanism* [23], introduces a new global anomalous symmetry which is then spontaneously broken at low energies, giving rise to the axion.

The effective potential of the action resembles, but crucially is not identical, to the one of a single cosine [24], as in an instanton solution. It's mass is approximately $m \sim \Lambda^2/f_\alpha$, where Λ is the QCD scale ~ 100 MeV and f_α is some high energy scale that suppresses the axion coupling. For example, for $f_\alpha \approx 10^{13}$ GeV, the axion mass is around $m_\alpha \approx 10^{-6}$ eV.

A generalization of the QCD axion is the class of the *axion-like particles* (ALPs). These are still pseudo-scalar bosons, but not tied to the QCD framework. They are mainly found in string theory and supersymmetry related concepts where multiple global symmetries can lead to ALP fields with small masses and weak couplings. Unlike the axion case, ALP masses are not directly related to coupling constants, which can be tuned separately. This allows ALPs to potentially occupy a vast parameter space, including the lowest boundary of WDM, which as we previously mentioned overlaps with the fuzzy dark matter.

1.3.2 Dark Photon

Despite the seemingly contradictive name, the *dark photon* is a massive spin-1 vector boson that arises in theories with an additional $U(1)'$ gauge symmetry in a hidden sector [25]. The dark photon couples very weakly to the Standard model with a process known as *kinetic mixing*, which introduces an interaction between the dark photon field A'_μ and the ordinary electromagnetic photon A_μ, via a term in the Lagrangian of the form

$$\mathcal{L} \supset \frac{\epsilon}{2} F^{\mu\nu} F'_{\mu\nu}, \tag{1.3}$$

where ϵ is the kinetic mixing parameter, $F^{\mu\nu}$ is the field strength tensor of electromagnetism, and $F'_{\mu\nu}$ is the field strength tensor of the dark photon. As WDM candidates, the masses of dark photons are ultralight and depend largely on the mixing parameter and the production mechanisms in the early universe. In general,

the dark photon belongs to a broader category of *vector wave dark matter* that could possibly interact with regular matter through interaction Lagrangian terms like $gA'_\mu \bar{\psi}\gamma^\mu\psi$, producing a detectable new kind of force (sometimes referred to as a *fifth force*), very similarly to the kind of dark matter this thesis investigates and will be discussed in the next section.

1.3.3 Scalar WDM

As the title of this thesis suggests, the focus of the model and theoretical calculations would be *scalar wave dark matter*. First of all, the ultra light dark matter already discussed has to be necessarily bosonic. Fermionic dark matter has to follow the *Pauli exclusion principle* meaning that in a given volume confined by the de Broglie wavelength, the particle number of Eq. (1.2) cannot be arbitrarily high. Thus, only a boson candidate can be approximated as a classical wave, a phenomenon very similar to the *Bose-Einstein condensation* that can manifest in bosonic matter under very low temperatures.

The simplest case of a boson, is a spin zero particle, that is associated with a *scalar* field. Besides the omission of spin effects, the spin-0 case also produces an experimentally desirable effect on interactions with matter. Specifically, as we will discuss analytically on the next chapter, scalar interactions result in time-dependent signals with the same frequency and phase as the dark matter field. For higher spins, this effect is only achievable in *minimal coupling* interactions with a spin-1 vector field [26] .

1.4 Motivation and aim of this thesis

The main goal of this thesis is to investigate the detection of scalar wave dark matter in the $10^{-14} - 10^{-12}$ eV area, through a future magnetic levitation experiment, utilizing a superconducting sphere as a sensor. Similar experiments have been proposed [27] to be conducted in Chalmers, mainly for a possible detection of axions, such as interactions through SM coupling to magnetic field of the levitation trap [28]. In fact, very recently the first kind of this type of experiment has been conducted in the Leiden University [29], which was aimed to detect vector wave dark matter in a very specific frequency range. Thus, the experiment studied theoretically in this thesis is realistically achievable with the current technology and research capability of the MC2 Quantum Technologies Lab in Chalmers. For the purpose of the numerical simulations employed in this thesis, every parameter estimation was done in consultation with researchers from the Wiezcorek lab [30].

The particular interaction that this thesis studies is the simplest, non-derivative interaction of the scalar wave dark matter and nucleons of the superconducting target, akin to Yukawa interactions e.g. the famous Higgs boson interaction. Derivative interactions are also possible but the target bodies are charge neutral and tend to have very low intrinsic spin to couple strongly with derivative terms in the Lagrangian. Furthermore, we are going to assume interactions only with neutrons. In general, this type of scalar interaction is allowed for protons just the same as it is with

neutrons. The reason we are going to refer only to neutrons is twofold: first we are going to show that the coupling is proportional to the neutron number, which if we also consider proton interactions can be easily rescaled to fit with the simulations i.e. $Ny_{\phi n} \to (N+Z)y_{\phi n}$. Since the number of protons Z is similar to the number of neutrons N in materials and the proton and neutron masses are nearly identical, the difference in rescaling will be close to just multiplying with a factor of 2. Other fermions, like electrons can also be included in this interaction [26] with terms like

$$\mathcal{L} \supset y_{\phi e}\phi\bar{\psi}_e\psi_e, \tag{1.4}$$

which could further change the normalization of the coupling studied in this thesis.

The second reason is that the most searched for coupling in proposed experiments of this type (or other types like optomechanic experiments [31]) is the vector wave dark matter coupling g_{B-L} to the *Baryon-Lepton number*, which is essentially a coupling to the neutron number (reasoning for this is presented thoroughly in [26], but is very close to a DM charge neutrality in the nucleus with neutrons being the exception). While this type of interaction is very different from the one studied in this thesis, it can be shown [32] that the final form of the interaction force differs only in a factor of velocity

$$g_{B-L} = v\ y_{\phi n}. \tag{1.5}$$

Thus, having $y_{\phi n}$ being only the neutron coupling model means we can easily compare sensitivity projections with just a re-scaling of the coupling based on the velocity suppression. Notably the first and currently only magnetic levitation experiment conducted [29] puts a constraint on the g_{B-L} and not $y_{\phi n}$.

2

Theory

In the following chapter we are going to derive the interaction force from fundamental theory. As discussed in the introduction chapter, only neutron interactions are going to be considered. A short discussion on the nature of the force will follow at the end of the chapter.

2.1 Scattering with neutrons

As a first step into calculating the force resulting from the wave-like DM and single neutron interaction, non-relativistic scattering theory techniques will be implemented. Summarizing the following calculation, the relations involving the S-matrix element of the interaction, both from the Quantum Mechanical and Quantum Field Theory formulation will be compared. The end result will the a relation between the interaction potential and the classical field components.

2.1.1 Harmonic perturbation

It is important to carefully account for the spatial and time dependence of the potential which in this case, as an ansatz, will be considered to have a separable harmonic time-dependent component. With that in mind, the Hamiltonian[1] of the problem is

$$H = H_0 + V_{\text{int}} = H_0 + Ve^{i\omega t} + V^\dagger e^{-i\omega t}, \tag{2.1}$$

where V and $V^\dagger$ are time-independent components of the interaction potential. In the interaction picture the time evolution of states is determined by

$$V_I(t, \vec{x}) = e^{iH_0 t}\left(V(\vec{x})e^{i\omega t} + V^\dagger(\vec{x})e^{-i\omega t}\right)e^{-iH_0 t} \tag{2.2}$$

where $V(\vec{x})$ and $V^\dagger(\vec{x})$ are defined in the Schroedinger picture. The time evolution operator U_I fulfills the Schroedinger equation

$$i\frac{\partial}{\partial t}U_I(t, t_0) = V_I(t)U_I(t, t_0)$$

with solution

[1] Usage of natural units $\hbar = c = 1$ will be common across the thesis, except when stated otherwise.

$$U_I(t,t_0) = 1 - i\int_{t_0}^{t} V_I(t')U_I(t',t_0)dt'$$

and transition amplitude

$$\langle f|\, U_I(t,t_0)\,|i\rangle = \delta_{fi} - i\int_{t_0}^{t}\langle f|\, V_I(t')U_I(t',t_0)\,|i\rangle\, dt'$$

where initial and final states $|i\rangle$ and $|f\rangle$ are eigenstates of the free hamiltonian H_0. Substituting (2.2) into the solution we get

$$\begin{aligned}\langle f \mid U_I(t,t_0) \mid i\rangle = \delta_{fi} &- i\sum_m \langle f \mid V \mid m\rangle \int_{t_0}^{t} e^{i\omega_{fi}t'+\omega t'}\langle m \mid U_I(t,t_0) \mid i\rangle dt' \\ &- i\sum_m \langle f \mid V^\dagger \mid m\rangle \int_{t_0}^{t} e^{i\omega_{fi}t'-\omega t'}\langle m \mid U_I(t,t_0) \mid i\rangle dt' \qquad (2.3)\end{aligned}$$

where $\omega_{fi} = E_f - E_i$. Recursive substitutions give a higher order solution to the same equation. It is useful to define the T-matrix element $T_{fi} = \langle f|\, T\,|i\rangle$ as

$$\langle f|U_I(t,t_0)|i\rangle = \delta_{fi} - iT_{fi}\int_{t_0}^{t} e^{i(\omega_{fi}+\omega)t'+\varepsilon t'}dt' - iT_{fi}^\dagger\int_{t_0}^{t} e^{i(\omega_{fi}-\omega)t'+\varepsilon t'}dt' \qquad (2.4)$$

where $\epsilon > 0$ is arbitrary small. Thus the definition of the S-matrix element is

$$\begin{aligned}S_{fi} &\equiv \lim_{t\to\infty}\left[\lim_{\varepsilon\to 0}\langle f \mid U_I(t,-\infty) \mid i\rangle\right] = \delta_{fi} - iT_{fi}\int_{-\infty}^{\infty} e^{i(\omega_{fi}+\omega)t'}dt' - iT_{fi}^\dagger\int_{-\infty}^{\infty} e^{i(\omega_{fi}-\omega)t'}dt' \\ &= \delta_{fi} - 2\pi\delta(E_f - E_i + \omega)iT_{fi} - 2\pi\delta(E_f - E_i - \omega)iT_{fi}^\dagger. \qquad (2.5)\end{aligned}$$

In our case we are going to rely on the first order of the recursive solution by setting

$$\langle f|\, T\,|i\rangle = \langle f|\, V\,|i\rangle$$

which is called the *first order Born approximation* of the S-matrix element

$$S_{fi}^{(1)} = -2\pi\delta(E_f - E_i + \omega)iV_{fi} - 2\pi\delta(E_f - E_i - \omega)iV_{fi}^\dagger \qquad (2.6)$$

where the trivial "no interaction" δ_{fi} factor is omitted and

$$V_{fi} = \langle f|\, V\,|i\rangle = \langle \vec{k'} \mid V \mid \vec{k}\rangle = \int d^3x\ \langle \vec{k'} \mid \vec{x}\rangle\langle \vec{x} \mid V \mid \vec{k}\rangle.$$

We treat V as a local potential, that is a potential diagonal to the $\vec{x}$ representation, essentially a function of $\vec{x}$, which means $\langle \vec{x'} \mid V \mid \vec{x''}\rangle = V(x')\delta^3(\vec{x'} - \vec{x''})$, thus

$$V_{fi} = \int d^3x\ \langle \vec{k'} \mid \vec{x}\rangle V(\vec{x})\langle \vec{x} \mid \vec{k}\rangle = \int d^3x\ e^{-i\vec{k'}\vec{x}}V(\vec{x})e^{i\vec{k}\vec{x}} = \tilde{V}(\vec{k} - \vec{k'}), \qquad (2.7)$$

similarly for the adjoint

$$\begin{aligned}V_{fi}^\dagger = \langle f|\, V^\dagger\,|i\rangle &= \langle i|\, V\,|f\rangle^* \qquad (2.8)\\ &= \int d^3x\ e^{-i\vec{k}\vec{x}}V^*(\vec{x})e^{i\vec{k'}\vec{x}} = \tilde{V}^*(\vec{k'} - \vec{k}). \qquad (2.9)\end{aligned}$$

Finally, equation (2.6) becomes

$$S_{fi}^{(1)} = -2\pi\delta(E_f - E_i + \omega)i\tilde{V}(\vec{k} - \vec{k'}) - 2\pi\delta(E_f - E_i - \omega)i\tilde{V}^*(\vec{k'} - \vec{k}) \tag{2.10}$$

So far our approach employed only non-relativistic relations found in Quantum Mechanics with first order approximations. To get an expression for V_{fi} we will need to calculate the first order S-matrix element within the framework of Quantum Field Theory.

2.1.2 Scattering with external classical scalar field

Consider the interacting Lagrangian density

$$\mathcal{L}_{\text{int}} = y_{\phi n}\phi\bar{\psi}\psi \tag{2.11}$$

describing the neutron-WDM interaction, with $y_{\phi n}$ coupling constant and ψ being the neutron fermionic field, in which WDM is a scalar *classical* field with a general time-dependent wave form

$$\phi(x) = \varphi(\vec{x})e^{i\omega t} + \varphi^*(\vec{x})e^{-i\omega t}, \tag{2.12}$$

that is a solution to the scalar field equation of motion, the *Klein-Gordon equation*

$$(\Box + m^2)\phi(x) = 0. \tag{2.13}$$

where φ is a complex scalar field. Taking into consideration that ψ and $\bar{\psi}$ are the only *quantum* fields in the interacting Lagrangian density, the first order S-matrix element is

$$S_{fi}^{(1)} = iy_{\phi n}\int d^4x \, \langle f|\underbrace{\bar{\psi}}\, \phi(x)\, \underbrace{\psi}|i\rangle$$

where the normalization of the state-field Wick contraction is set to be

$$\underbrace{\psi(x)}|i\rangle = \underbrace{\psi(x)|}\, \vec{k}, s\rangle = e^{-ikx}u^s(k)|0\rangle,$$

for neutron with initial momentum $\vec{k}$ and spin s. Similar normalization is set for the final state Wick contraction. The S-matrix element is then

$$S_{fi}^{(1)} = iy_{\psi n}\int d^4x \; e^{ik'x}\phi(x)e^{-ikx}\bar{u}^{s'}(k')u^s(k)\,\langle 0|0\rangle\,,$$

where the spinor product is calculated under a non-relativistic convention where the spinors are normalized as

$$u^s(p) = \frac{1}{\sqrt{2}}\begin{pmatrix}\xi^s \\ \xi^s\end{pmatrix},$$

with ξ^s being a two-component constant spinor normalized to $\xi^{s'\dagger}\xi^s = \delta^{ss'}$. Thus

$$\bar{u}^{s'}(k')u^{s}(k) = \delta^{ss'} = 1,$$

since the interaction of the unpolarized neutrons with the spin-less field ϕ will not affect their spin state. The S-matrix element is then

$$\begin{aligned} S_{fi}^{(1)} &= iy_{\psi n} \int d^4x \; e^{ik'x}\phi(x)e^{-ikx} \\ &= iy_{\psi n} \int d^4x \; e^{ik'x} \left(\varphi(\vec{x})e^{i\omega t} + \varphi^*(\vec{x})e^{-i\omega t}\right) e^{-ikx}. \end{aligned} \tag{2.14}$$

This expression can be written in a form resembling to equation (2.6) as

$$\begin{aligned} S_{fi}^{(1)} = iy_{\psi n} \Bigg[& 2\pi\delta(E' - E + \omega) \int d^3x \; e^{-i\vec{k'}\cdot\vec{x}}\varphi(\vec{x})e^{i\vec{k}\cdot\vec{x}} \\ & + 2\pi\delta(E' - E - \omega) \int d^3x \; e^{-i\vec{k'}\cdot\vec{x}}\varphi^*(\vec{x})e^{i\vec{k}\cdot\vec{x}} \Bigg]. \end{aligned} \tag{2.15}$$

The integrals above are the Fourier transformations of spatial parts $\varphi(\vec{x})$ and $\varphi^*(\vec{x})$ to momentum space, denoted as $\tilde{\varphi}(\vec{k} - \vec{k'})$ and $\tilde{\varphi}^*(\vec{k} - \vec{k'})$, thus

$$S_{fi}^{(1)} = iy_{\psi n}\Big[2\pi\delta(E' - E + \omega)\tilde{\varphi}(\vec{k} - \vec{k'}) + 2\pi\delta(E' - E - \omega)\tilde{\varphi}^*(\vec{k} - \vec{k'})\Big]. \tag{2.16}$$

At this point we shall consider the case that $\phi(x)$ is a *real* scalar field, meaning that the solution (2.12) is a real plane-wave solution in the form (up to a random phase)

$$\phi(x) = \phi_0 \cos\left(\omega t - \vec{p}\cdot\vec{x}\right) = \frac{\phi_0}{2}\left(e^{i\omega t}e^{-i\vec{p}\cdot\vec{x}} + e^{-i\omega t}e^{i\vec{p}\cdot\vec{x}}\right)$$

meaning that

$$\varphi(\vec{x}) = \frac{\phi_0}{2}e^{-i\vec{p}\cdot\vec{x}} \quad \text{and} \quad \varphi^*(\vec{x}) = \frac{\phi_0}{2}e^{i\vec{p}\cdot\vec{x}}. \tag{2.17}$$

Direct calculation of the Fourier transformations of equation(2.16) gives

$$S_{fi}^{(1)} = iy_{\psi n}\frac{\phi_0}{2}\Big[2\pi\delta(E'-E+\omega)(2\pi)^3\delta(\vec{k}-\vec{k'}+\vec{p})+2\pi\delta(E'-E-\omega)(2\pi)^3\delta(\vec{k}-\vec{k'}-\vec{p})\Big].$$

With the delta functions enforcing energy and momentum conservation, we can interpret the first term as neutron-WDM scattering that transfers energy to the target object, while the second term represents a scattering process where the target object loses energy to the environment.
Comparing equation(2.10) and equation(2.16) gives

$$\tilde{V}(\vec{k} - \vec{k'}) = -y_{\phi n}\tilde{\varphi}(\vec{k} - \vec{k'}) \tag{2.18}$$

Applying the reverse Fourier transform we finally get the time-independent potential components in position space

$$V(\vec{x}) = -y_{\phi n}\varphi(\vec{x}) = -y_{\phi n}\frac{\phi_0}{2}e^{-i\vec{p}\cdot\vec{x}}, \tag{2.19}$$

$$V^{\dagger}(\vec{x}) = -y_{\phi n}\varphi^{*}(\vec{x}) = -y_{\phi n}\frac{\phi_0}{2}e^{i\vec{p}\cdot\vec{x}}. \tag{2.20}$$

Finally, the time-dependent interaction potential is

$$V_{\text{int}}(\vec{x},t) = -y_{\phi n}\frac{\phi_0}{2}\left(e^{i(\omega t-\vec{p}\cdot\vec{x})} + e^{-i(\omega t-\vec{p}\cdot\vec{x})}\right) = -y_{\phi n}\phi_0\cos(\omega t - \vec{p}\cdot\vec{x}). \tag{2.21}$$

2.1.3 Force on a single neutron

The force induced from the interaction can be easily obtained from the classical definition of the force as the negative gradient of the interaction potential

$$\vec{F}_{\text{int}} = -\boldsymbol{\nabla}V_{\text{int}}(\vec{x},t) \tag{2.22}$$

$$= -\vec{p}\, y_{\phi n}\phi_0\sin(\omega t - \vec{p}\cdot\vec{x}). \tag{2.23}$$

Next, an approximate relation between the field amplitude ϕ_0 and the wave DM density ρ_{DM} will be demonstrated. Consider the stress-energy tensor

$$T^{\mu\nu} = \frac{\partial\mathcal{L}}{\partial(\partial^{\mu}\phi)}\partial_{\nu}\phi - g_{\mu\nu}\mathcal{L} \tag{2.24}$$

$$= g^{\mu\nu}\partial_{\nu}\phi\partial^{\nu}\phi - g^{\mu\nu}\mathcal{L}. \tag{2.25}$$

where the density of matter is given by the time-like component

$$\begin{aligned}\rho = T_{00} &= \dot{\phi}^2 - \frac{1}{2}\partial_{\mu}\phi\partial^{\mu}\phi + \frac{1}{2}m_{\phi}^2\phi^2 \\ &= \frac{1}{2}\dot{\phi}^2 + \frac{1}{2}(\nabla\phi)^2 + \frac{1}{2}m_{\phi}^2\phi^2.\end{aligned} \tag{2.26}$$

Substituting with the plain wave $\phi(x) = \phi_0\cos(\omega t - \vec{p}\cdot\vec{x})$ and taking into account the $m_{\phi} \approx \omega$ approximation, we get

$$\begin{aligned}\rho &= \frac{1}{2}\Big[(m_{\phi}\phi_0\sin(\omega t - \vec{p}\cdot\vec{x}))^2 + (p\phi_0\sin(\omega t - \vec{p}\cdot\vec{x}))^2 \\ &\qquad + (m_{\phi}\phi_0\cos(\omega t - \vec{p}\cdot\vec{x}))^2\Big] \\ &= \frac{1}{2}\Big[m_{\phi}^2\phi_0^2 + p^2\phi_0^2\sin^2(\omega t - \vec{p}\cdot\vec{x})\Big]\end{aligned} \tag{2.27}$$

where we can just write the momentum carried by the DM wave non-relativistically as $p = m_\phi v$, where v is the velocity. Thus, the average DM density along a period $2\pi/\omega$ is

$$\langle \rho_{\rm DM} \rangle = \frac{1}{2} m_\phi^2 \phi_0^2 (1 + v^2), \tag{2.28}$$

where in the non-relativistic limit (e.g. $v \approx 10^{-3}$) we have (dropping the average notation)

$$\rho_{\rm DM} = \frac{1}{2} m_\phi^2 \phi_0^2. \tag{2.29}$$

It's worth noting that if we also take into account that the spatial variation of the DM wave near the target object of the interaction is negligible, then the gradient of equation(2.26) becomes zero and the result is still the same.

Substituting into equation (2.23), the force expression becomes

$$\vec{F}_{\rm int} = -\frac{\vec{p}}{m_\phi} y_{\phi n} \sqrt{2\rho_{\rm DM}} \sin(\omega t - \vec{p} \cdot \vec{x}), \tag{2.30}$$

where $\vec{p}$ and m_ϕ are the momentum and mass carried by the DM wave. The force vector has the direction of the gradient of the field, which is the momentum $\vec{p} = m_\phi \vec{v}$. Normally the velocity v of WDM, being the velocity of many waves in superposition, is distributed according to a Boltzmann distribution. However, for reasons of simplicity and computational cost effectiveness we are going to consider the velocity constant $v = 10^{-3}$. This is a typical velocity for DM that is assumed to move according to the *Virial theorem* in the Galaxy.

2.2 EP violation

The calculated force is characterized as an *EP-violating* force and in this section we shall explain and motivate this terminology.

Formally, the *Equivalence Principle* (EP) states that for each space-time point X one can introduce a coordinate system ξ_X^α with $X = 0, ...$ such that in a neighborhood of X the laws of physics are the ones of special relativity in the absence of gravity. In other words, in any and every locally inertial frame the laws of special relativity must hold. If we restrict the statement for only the "laws of free falling bodies" instead of "all laws of nature" then we refer to the *Weak Equivalency Principle* (WEP).

To illustrate the EP, the famous elevator example is often used, but in our case it would be better to just state the Newtonian implication the EP has: Gravity couples with mass as its charge, as we know gravity is a force proportional to the mass of the object that is attracted. Also, the inertial mass is the measure of the objects acceleration, as stated in Newton's second law. Thus, the EP implies that these two masses are the same thing and in a uniform gravitational field, all objects fall with the same acceleration near the surface of the earth.

One can observe similarities with our calculated interaction force on a single neutron and gravity. If we want to write the total force on a massive object, having N amount of neutrons, then using equation (2.30) and assuming constant velocity we have

$$|F_{\text{int}}| \propto N v y_{\phi n} \sqrt{2\rho_{\text{DM}}}, \tag{2.31}$$

however N is not precisely proportional to the mass of the object and differs lightly depending on the material the target is made of (one can approximate $N \sim m/2m_n$m where m is the mass of the target and m_n the neutron mass). This the interaction force would produce a relative acceleration on objects made of different materials, in complete contrast with gravity. In our case this is easily understood since N is the neutron number due to the fact that we only consider neutron interactions, but this is a signature feature of scalar wave dark matter interactions and can be shown for several kinds of scalar interaction terms, like Higgs-portal interactions or electron mass couplings [26]. The relative acceleration is a useful feature but not a necessary one for the detection scheme that we will introduce in the next chapter. In fact gravity can be detected, an EP preserving force, just the same. The EP-violating feature would be more useful if one considers an array of sensors with different materials and observes the difference in acceleration in a fixed frame.

3

Model

The specifics of the model are going to be analysed in this chapter. The physics behind the levitation of the superconductor are going to be briefly introduced and the parametrization of the detection scheme is going to be presented. The expressions shown for the noise sources are going to be included to the model and will be crucial for the next chapter.

3.1 Magnetically Trapped Superconductor

The macroscopic phenomenon of magnetic levitation is possible due to the quantum mechanical properties of a superconductor. A superconductor, when cooled below its critical temperature T_c, exhibits zero electrical resistance and expels magnetic fields from its interior[1], an effect known as the *Meissner effect* that stems from the fact that inside a perfect superconductor there cannot exist a non-zero uniform magnetic field [33]. If the external magnetic field reaches a critical point, it can fully penetrate the superconductor, essentially turning it back to "normal".

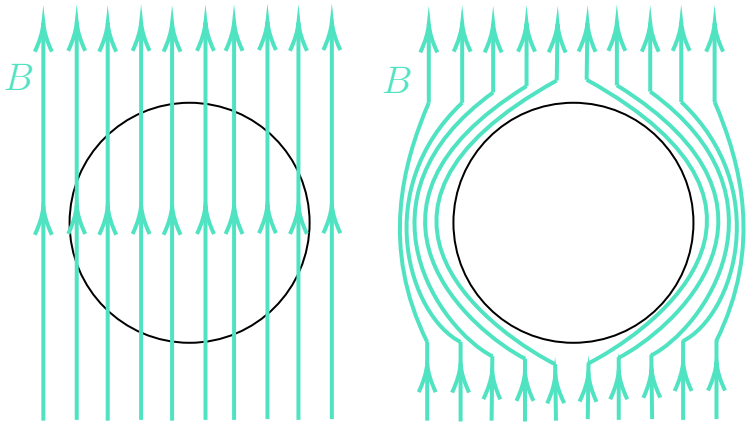

Figure 3.1: Illustration of the Meissner effect. A spherical conductor above critical temperature (left) allows uniform magnetic field inside, whereas below that critical temperature it expels magnetic lines (right).

Inside a magnetic field, a superconductor needs to overcome the force of gravity to be levitated and somehow be also stable. In other words, in a magnetic trap a restoring

[1]Superconductors exhibit a finite depth through which a magnetic field can penetrate their surface. This is the *London penetration depth*, typically around the order of 10 nanometers.

force would need to oppose external forces that displace the superconductor. Consider a setup similar to Figure 3.2 where a spherical type I superconductor is cooled below T_c and placed between an anti-Helmholtz-like configuration and aligned with the center of the setup where the magnetic field would be zero.

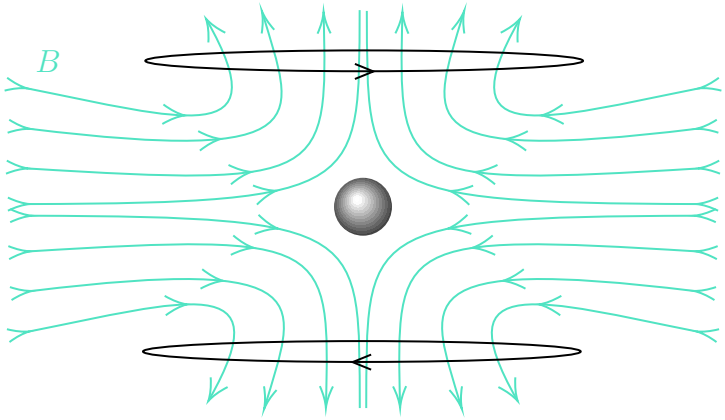

Figure 3.2: Illustration of a magnetic trap. A superconducting sphere (type-I superconductor) is placed at the center of a levitation apparatus that consists of two current-carrying coils arranged in an anti-Helmholtz-like configuration, i.e., carrying currents in opposite directions.

Any external force acting on the sphere would displace it from the center of zero magnetic field. For example, gravity would displace the sphere downwards. Linear expansion of the magnetic field near the center gives

$$B_j(x) = \left.\frac{\partial B_i}{\partial x_j}\right|_{x=0} x_j, \quad i,j = 1,2,3. \tag{3.1}$$

The displaced superconductor would expel the magnetic field lines of equation (3.1) by creating screening currents along its surface (see Figure 3.3).
The specific mechanism that expels the magnetic field lines from the superconductor's interior is the screening magnetic field generated by screening currents along its surface. It can be shown (see [28]) that the total magnetic field induces a net Lorentz force on the superconducting sphere, opposing the displacement caused by the external force. This force acts as a restoring force of the form

$$F_{\text{trap},j} = -\frac{3}{2} V B_j \left(\frac{\partial B_j}{\partial x_i}\right)_{x_i=0}, \tag{3.2}$$

where V is the volume of the superconducting sphere. Combining equation (3.1) and equation (3.2) we have

$$F_{\text{trap},j} = -\frac{3}{2} V (\partial_i B_j)(\partial_j B_i) x_j, \tag{3.3}$$

thus for an external force of random direction, the opposing restoring force is

$$\vec{F}_{\text{trap}} = -\frac{3}{2} V \left((\partial_x B_x)^2 x\hat{x} + (\partial_y B_y)^2 y\hat{y} + (\partial_z B_z)^2 z\hat{z}\right) \tag{3.4}$$

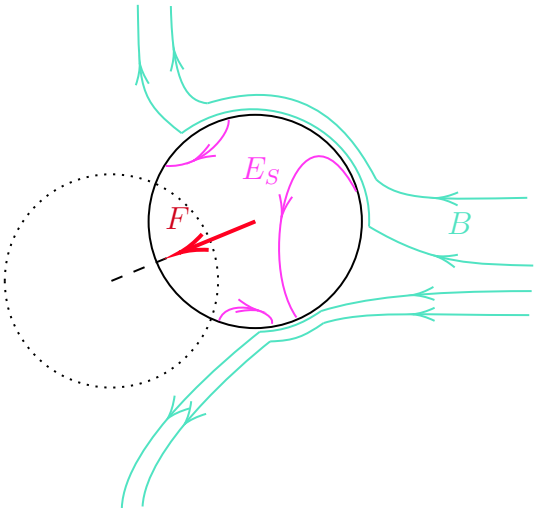

Figure 3.3: If the superconductor is displaced from the center, screening currents (violet) will run on the surface of the sphere to screen the magnetic field (blue) of the trap of its interior. The total magnetic field will induce a net Lorentz for on the currents that will act as a restoring force (red).

where $\partial_i B_j = \frac{\partial B_i}{\partial x_j}\Big|_{x=0}$ is diagonal. It is apparent from the form of the restoring force that the system acts as a harmonic oscillator with equilibrium at $x_i = 0$. The resonant frequencies of the trap are given by [27]

$$f_i = \partial_i B_i \sqrt{\frac{3}{8\pi^2 \rho}} \tag{3.5}$$

where ρ is the density of the sphere. It is important to note that since the gravitational force on the sphere is constant the equilibrium would be displaced by z', where by equating the weight with equation (3.2)

$$-mg\hat{z} = -\frac{3}{2} V (\partial_z B_z)^2 z' \hat{z} \tag{3.6}$$

and substituting the resonant frequencies from equation (3.5) we have

$$z' = \frac{g}{4\pi f_i^2}. \tag{3.7}$$

The equilibrium displacement is thus dependent on the resonant frequencies f_i and is around 0.08 mm for $f_0 = 100$ Hz.

3.2 Coupled Oscillator Parametrization

A simplistic, one-dimensional model regarding the magnetic trap of the previous section would be a harmonic oscillator tied in a platform where the anti-Helmholtz setup is mounted. In a realistic lab setup strong vibrations would influence the movement of the levitated object, thus the platform is hung from a base by a spring of different natural frequency in order to shield the platform and by extension the levitated object from unwanted vibration noise.

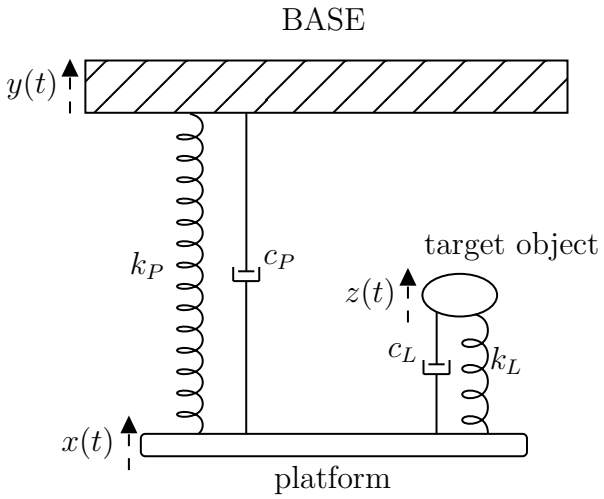

Figure 3.4: Coupled oscillator setup as a one dimensional parametrization of a magnetically trapped superconductor, shielded from environmental vibrations. The base is generating the vibrations since it is connected to the Earth. Displacement coordinates $x(t), y(t), z(t)$ have their direction indicated.

This coupled oscillator setup, visualized in Figure (3.4), is the basis of the numerical model of this thesis. The equations of motion for the levitated object are

$$\begin{aligned} m_p\ddot{x}(t) = &-k_p\left(x(t)-y(t)\right) - c_p\left(\dot{x}(t)-\dot{y}(t)\right) \\ &+ k_l\left(z(t)-x(t)\right) + c_l\left(\dot{z}(t)-\dot{x}(t)\right) - F_p^{\mathrm{DM}}, \end{aligned} \tag{3.8}$$

$$m_l\ddot{z}(t) = -k_l\left(z(t)-x(t)\right) - c_l\left(\dot{z}(t)-\dot{x}(t)\right) - F_l^{\mathrm{DM}}. \tag{3.9}$$

where p, l indices refer to the platform and levitated object respectively and $k_{p,l}$ is the stiffness of the spring, $c_{p,l}$ is the damping constant and $F_{p,l}^{\mathrm{DM}}$ is the dark matter force acting on the whole of the platform or levitated object. The right hand side terms on Eqs. (3.8) and (3.9) are the forces applied on each massive object, found by application of Newton's second law, which are the tension of the spring and the damping force, with the respective reaction, or back-action, terms in equation (3.8).

Dividing each equation with the mass $m_{p,l}$ of platform/levitated object, gives a DE system

$$\begin{aligned} \ddot{x}(t) = &-\omega_p^2\left(x(t)-y(t)\right) - \gamma_p\left(\dot{x}(t)-\dot{y}(t)\right) \\ &+ \frac{m_l}{m_p}\omega_l^2\left(z(t)-x(t)\right) + \frac{m_l}{m_p}\gamma_l\left(\dot{z}(t)-\dot{x}(t)\right) - \frac{F_p^{\mathrm{DM}}}{m_p}, \end{aligned} \tag{3.10}$$

$$\ddot{z}(t) = -\omega_l^2\left(z(t)-x(t)\right) - \gamma_l\left(\dot{z}(t)-\dot{x}(t)\right) - \frac{F_l^{\mathrm{DM}}}{m_l}, \tag{3.11}$$

with the suitable experimental parameters

$$\omega_i = \sqrt{\frac{k_i}{m_i}}, \quad \gamma_i = \frac{c_i}{m_i}. \tag{3.12}$$

It is worth noting that the m_l/m_p mass ratio would in general be extremely small, e.g. $\simeq \mathcal{O}(-10)$, since the levitated object's scale would be on the micro meter side. That would make the effect of the levitation back-action on the platform almost negligible, however the numerical simulations done when ignoring these terms showed that unwanted nonlinearities become prominent and a very small but noticeable resonance peak frequency shift appeared.

Considering the result of equation (2.30), the DM force on the whole material that is either platform or levitated object is proportional to the number of neutrons N of the material, thus

$$F_{p,l}^{\mathrm{DM}} = N_{p,l} F_{\mathrm{int}} = N_{p,l}\, v y_{\phi n} \sqrt{2\rho_{\mathrm{DM}}} \sin(\omega t - \vec{p}\cdot\vec{x}) \tag{3.13}$$

where the spatial dependency is dropped from the force expression. One can see that for example, considering DM mass of 10^{-12} eV, the momentum is $p = 10^{-15}$ eV and the de Broglie wavelength is $\lambda_{dB} = 2\pi \times 10^{15}$ eV$^{-1} = 6.2 \times 10^{9}$ m, which is way higher than the scale of the experiment.

3.2.1 Modeling the vibrational noise

Since the coupling of the neutron-WDM interaction is supposed to be extremely weak, the amplitude of the DM force acting on the target object is also expected to be weak. As a result, the vibrational noise effect becomes significant compared to the effect of the DM force on the acceleration of the levitated object.

To start, the vibrational noise $\epsilon(t)$ is linked to the position of the base $y(t) = y_0 + \epsilon(t)$ where the initial condition y_0 is set to zero. This means that $y(t)$ is not going to be treated as a dynamical variable of the DE system, since it's time evolution will be determined solely by the vibrational noise. Modeling the vibrational noise requires us first to define a power spectral density function (PSD) S_{yy}, which characterizes how the power of a signal (in this case ground vibrations) is distributed across different frequency components. The preferred PSD for this model is

$$S_{yy}(\omega) = \delta \left(\frac{2\pi}{\omega}\right)^4, \tag{3.14}$$

where $\delta = 10^{-10}$ m^{2}Hz^3. Additionally, in order to simplify the model further we are going to assume that the noise is flattened for lower frequencies, setting the boundary at 0.5 Hz.

Since $y(t)$ is not going to be analytically defined by the DE system we are going to construct it as a sum of sinusoidal components

$$y(t) = \sum_{i=0}^{N-1} \sqrt{2 S_{yy} \Delta\omega} \sin(\omega_i t + \phi_i), \tag{3.15}$$

with amplitudes determined by the prescribed PSD, where $\Delta\omega$ is the frequency spacing between successive components and ϕ_i is a random phase assigned to each

component. Using a sampling of frequencies, chosen randomly over a uniform distribution together with a uniform distribution of random phases, we can determine a single realization of $y(t)$ using equation (3.15). A single realization of $y(t)$ is going to be fed into Eqs. (3.10, 3.11), that are going to be solved numerically for $z(t)$. The process is repeated for another new realization of $y(t)$ through a *Monte Carlo loop* that is going to give as a set of multiple solutions of $z(t)$.

3.2.2 Thermal noise and effective temperature

Any movement, either due to external vibrations or exposure to environmental radiation or particles, will give rise to thermal noise in the model. Environmental thermal fluctuations for example, is an ever present noise source that defines an irreducible floor for any measurement.

The relation between the environment and a dissipative oscillator as in our case can be understood via the fluctuation–dissipation theorem (FTD), which states that when there is a process that dissipates energy, turning it into heat, there is a reverse process related to thermal fluctuations. In a state of thermal equilibrium, the environment induces an external force to the system, that results in equilibrium fluctuations. In a simplified and strictly classical case, when the system in focus is just the levitated object in a magnetic trap, i.e. the system is just a single harmonic oscillator with damping γ_l, the FTD implies that

$$S_{\mathrm{FF}}^{th} = 4\gamma_l m_l k_B T, \tag{3.16}$$

where T is the temperature of the environment (around the order of 10mK in superconductor levitation). A more useful quantity for our model would be the PSD of the displacement (noted as the general coordinate x here) due to thermal fluctuations, which is given by

$$S_{xx}^{th}(\omega) = |\chi(\omega)|^2 S_{FF}^{th}, \tag{3.17}$$

where the mechanical susceptibility $\chi(\omega)$ to the external thermal force is given by

$$\chi(\omega) = \frac{1}{m_l(\omega_l^2 - \omega^2 + i\gamma_l\omega)}. \tag{3.18}$$

Substituting equation (3.18) and equation (3.16) into equation (3.17) results in

$$S_{xx}^{th}(\omega) = \frac{4\gamma_l k_B T}{m_l((\omega_l^2 - \omega^2)^2 - \gamma_l^2\omega^2)} \tag{3.19}$$

equation (3.19) describes the PSD of the thermal fluctuations in the movement of a target object in a one dimensional damped harmonic oscillator. Our system though differs from this simplistic case, since it is coupled to another oscillator that induces external vibrations into the target's oscillation. These vibrations, like any other source of heat, produce energy that can be turned into heat due to damping. A relevant question would be: how does the effective temperature from the vibrational energy compare to the temperature of the environment?

3.2.2.1 Equipartition in a harmonic oscillator

Before doing any kind of numerical calculation, one way that we could answer that question would be to get an, approximate, analytical expression for the average internal energy of the target due to it's harmonic oscillation, in the absence of any other external signal except the vibrations from the base, an then turn it into effective temperature. For that purpose we are going to use the *equipartition theorem* which relates the effective temperature in an harmonic oscillator with it's potential energy as

$$\frac{1}{2}k_l\langle z^2\rangle = \frac{1}{2}k_B T_{\text{eff}}, \tag{3.20}$$

meaning that we will need to calculate $\langle z^2\rangle$ first. It's worth noting that we can also use the mean square velocity relation implied by the equipartition theorem that can also give us the effective temperature as

$$\frac{1}{2}m_l\langle \dot{z}^2\rangle = \frac{1}{2}k_B T_{\text{eff}}. \tag{3.21}$$

Both $\langle z^2\rangle$ and $\langle \dot{z}^2\rangle$ can be calculated similarly to arrive at the effective temperature but we shall choose to continue with the former, since despite the calculation and later numerical integration being purely theoretical, the quantity directly measured in the levitation experiment would always be the position of target instead of its velocity.

3.2.2.2 Analytical calculation of the transfer function

A good place to start would be equation (3.11) for $F_l^{DM} = 0$

$$\ddot{z}(t) = -\omega_l^2\Big(z(t) - x(t)\Big) - \gamma_l\Big(\dot{z}(t) - \dot{x}(t)\Big), \tag{3.22}$$

taking the Fourier transformation, we have

$$(i\omega)^2\tilde{z}(\omega) = -(\omega_l^2 + \gamma_l i\omega)(\tilde{z}(\omega) - \tilde{x}(\omega)) \tag{3.23}$$

$$\tilde{z}(\omega) = \frac{\omega_l^2 + i\gamma_l\omega}{\omega_l^2 - \omega^2 + i\gamma_l\omega}\tilde{x}(\omega). \tag{3.24}$$

Thus, the susceptibility is

$$\chi(\omega) = \frac{\omega_l^2 + i\gamma_l\omega}{\omega_l^2 - \omega^2 + i\gamma_l\omega}. \tag{3.25}$$

Next, we will calculate the transfer function (from $y(t)$ to $z(t)$), which is defined as

$$G(\omega) = \frac{\tilde{z}(\omega)}{\tilde{y}(\omega)} = \chi(\omega)\frac{\tilde{x}(\omega)}{\tilde{y}(\omega)}. \tag{3.26}$$

For that, we start as before from equation (3.10) with $F_p^{DM} = 0$

$$\ddot{x}(t) = -\omega_p^2 \left(x(t) - y(t)\right) - \gamma_p \left(\dot{x}(t) - \dot{y}(t)\right) + \frac{m_l}{m_p}\omega_l^2 \left(z(t) - x(t)\right) + \frac{m_l}{m_p}\gamma_l \left(\dot{z}(t) - \dot{x}(t)\right) \tag{3.27}$$

then, taking the Fourier transformation, we have

$$-\omega^2\tilde{x}(\omega) = -(\omega_p^2 + i\omega\gamma_p)(\tilde{x}(\omega) - \tilde{y}(\omega)) + \frac{m_l}{m_p}(\omega_l^2 + i\omega\gamma_l)(\tilde{z}(\omega) - \tilde{x}(\omega)), \tag{3.28}$$

doing some rearranging, the above equation becomes

$$\left(\omega_p^2 - \omega^2 + i\omega\gamma_p + \frac{m_l}{m_p}(\omega_l^2 + i\omega\gamma_l)\right)\tilde{x}(\omega) - \frac{m_l}{m_p}(\omega_l^2 + i\omega\gamma_l)\tilde{z}(\omega) = (\omega_p^2 + i\omega\gamma_p)\tilde{y}(\omega) \tag{3.29}$$

Substituting the equation (3.24) into the above, we have

$$\left(\omega_p^2 - \omega^2 + i\omega\gamma_p + \frac{m_l}{m_p}(\omega_l^2 + i\omega\gamma_l)\right)\tilde{x}(\omega) - \frac{m_l}{m_p}(\omega_l^2 + i\omega\gamma_l)\frac{\omega_l^2 + i\gamma_l\omega}{\omega_l^2 - \omega^2 + i\gamma_l\omega}\tilde{x}(\omega) = (\omega_p^2 + i\omega\gamma_p)\tilde{y}(\omega), \tag{3.30}$$

or

$$\tilde{x}(\omega) = \frac{(\omega_p^2 + i\gamma_p\omega)(\omega_l^2 - \omega^2 + i\gamma_l\omega)}{(\omega_p^2 - \omega^2 + i\gamma_p\omega)(\omega_l^2 - \omega^2 + i\gamma_l\omega) - \omega^2\frac{m_l}{m_p}(\omega_l^2 + i\gamma_l\omega)}\tilde{y}(\omega), \tag{3.31}$$

thus, the transfer function is

$$G(\omega) = \frac{(\omega_p^2 + i\gamma_p\omega)(\omega_l^2 + i\gamma_l\omega)}{(\omega_p^2 - \omega^2 + i\gamma_p\omega)(\omega_l^2 - \omega^2 + i\gamma_l\omega) - \omega^2\frac{m_l}{m_p}(\omega_l^2 + i\gamma_l\omega)}. \tag{3.32}$$

Having an analytical expression for the transfer function $G(\omega)$, we can proceed with the calculation of $\langle z^2 \rangle$. For that purpose, we are going to make use of the *Wiener-Khinchin theorem*, a foundational theorem for stochastic processes. According to the theorem, for a general x stationary random process the autocorrelation function

$$R_{xx} = \langle x^*(t)x(t+\tau)\rangle \tag{3.33}$$

can be expressed as the inverse Fourier transform of the power spectral density $S(f)$, given by

$$R_{xx} = \int_{-\infty}^{+\infty} e^{2\pi i\tau f} S(f) df. \tag{3.34}$$

In our case, the process $z(t)$ can be considered stationary since the damping coefficients γ_l and γ_p are time independent, there are no significant nonlinearities in the

behavior of the system and the external environment is in thermal equilibrium. By applying equation (3.34) we have

$$R_{zz}(\tau) = \int_{-\infty}^{+\infty} e^{2\pi i \tau \omega} S_{zz}(\omega) d\omega, \tag{3.35}$$

and by taking $\tau = 0$ in equation (3.33) we can get the mean squared displacement

$$\langle z^2 \rangle = R_{zz}(0) = \int_0^{\infty} S_{zz}(\omega) d\omega. \tag{3.36}$$

The displacement PSD S_{zz} can be found by using equation (3.26) to get the relation between displacement z and y coordinate noise as

$$S_{zz}(\omega) = |G(\omega)|^2 S_{yy}(\omega). \tag{3.37}$$

The above is essentially an analytical expression of the $S_{zz}^{\text{vib}}(\omega)$, which as explained in section 3.2.1, is modeled after stochastic noise in our noise analysis, through Monte Carlo simulations. Nevertheless, we can use the complex analytical form of equation (3.37) to get a different estimation of $\langle z^2 \rangle$, which can be also inferred from the simulated mean displacement, which will be discussed in the next chapter of this thesis.

The integral of equation(3.36) takes the form

$$\langle z^2 \rangle = \int_0^{\infty} |G(\omega)|^2 S_{yy}(\omega) d\omega, \tag{3.38}$$

which can be numerically computed since equation (3.32) and equation (3.14) give us analytical expressions for $G(\omega)$ and $S_{yy}(\omega)$. Having a value for $\langle z^2 \rangle$ means we can simply take equation (3.21) and find the effective temperature to be

$$T_{\text{eff}} = \frac{k_l \langle z^2 \rangle}{k_B}. \tag{3.39}$$

In calculating the effective temperature with the above formalism we only took into account the vibrational noise as the main source of noise in the displacement of the target object. While the exact motivation behind this lies in the order of parameters, specifically δ of the vibrational noise PSD, the additional noise sources would certainly effect the magnitude of the effective temperature.

3.2.3 Readout and measurement noise

As discussed, the DM-induced signal will exert a force on the levitated superconducting sphere, causing it to move and create a local distortion on the magnetic field of the trap, due to the previously mentioned expulsion of the internal magnetic field of the target object. This distortion can be measured and in fact will be the quantity that will give us information about the actual displacement of the target object from it's levitation equilibrium.

Naturally, we expect the displacement to be extremely minimal, whether it will come from external noise or the DM-signal itself. Thus a device capable of measuring extremely small changed in magnetic flux is needed, which in these kinds of

levitated experiments is usually chosen to be the *SQUID (Superconducting QUantum Interference Device)*. The physics, usage, applications and calibration of such a device are very interesting topics which will not be covered in this thesis, but, in general, the SQUID is mostly used as an astoundingly precise magnetometer, capable of detecting magnetic flux changes on the order of $10^{-6} - 10^{-7}\,\Phi_0$, where Φ_0 is the internal magnetic flux quantum ($\approx 2.07 \times 10^{-15}$ Wb). This leads to a sensitivity of, even as low as, 1 femtotesla, depending on the exact setup.

The coupling between the levitated superconducting sphere and the SQUID will be parametrized with the variable η, which can be varied according to the specific setup used. For example, a pick-up coil can be placed near the magnetic trap in order to detect the changes in the magnetic field and carry the flux to the SQUID, since setting a SQUID directly by the side of the levitated object would be realistically unfeasible. This "imprecision" in the setup creates the additional noise source to the position of the target object, referred to as imprecision noise, given by

$$S_{zz}^{\text{imp}}(\omega) = \frac{S_{\Phi\Phi}(\omega)}{\eta^2} \tag{3.40}$$

where $S_{\Phi\Phi}$ is the internal flux noise of the SQUID.

There is another, final, noise source that needs to be considered, called *measurement noise.* In every quantum system, the very act of measuring any given observable will result in some kind of "back-action" by the system. While the target object cannot be considered a quantum system due to it's micrometer scale, the SQUID is fundamentally a quantum system coupled to it. Thus the measurement itself would create a reaction of the measuring device that can effect the position of the target object. Specifically, the distortion of the magnetic field would be carried to the measuring device and create a current J in the superconducting loop of the SQUID. In turn, that current would create local magnetic fields of its own, that would counter-react on the levitated object with a force $-\eta J$. Thus, by taking the magnetic trap force expression (equation (3.2)), the magnetic field back-action noise is given by

$$S_{BB}^{\text{back}}(\omega) = \frac{4\eta^2 S_{JJ}(\omega)}{9V^2(\partial B)^2}, \tag{3.41}$$

where the notation means $(\partial B)^2 = (\partial_i B_j)(\partial^i B^j)$. As before, we would need to convert this to position noise, given by

$$S_{zz}^{\text{back}}(\omega) = |\chi(\omega)|^2 S_{FF}^{\text{back}}(\omega) = |\chi(\omega)|^2 \frac{9}{4} V^2 (\partial B)^2 S_{BB}^{\text{back}}(\omega), \tag{3.42}$$

where the susceptibility $\chi(\omega)$ is given by equation (3.18), since we are concerned only about the measurement back-action on the levitated object system and not the whole coupled oscillator setup. The back-action noise in the position in thus

$$S_{zz}^{\text{back}}(\omega) = \eta^2 |\chi(\omega)|^2 S_{JJ}(\omega). \tag{3.43}$$

Comparing equation (3.40) and equation (3.43) one would notice a completely inverse dependency on the square of the η parameter. This signals a trade-off when

choosing the η parameter, between the readout-related noise and the noise from the quantum measurement. We can parametrize these two noise terms further by introducing the experimental parameters

$$\kappa = \sqrt{S_{JJ} S_{\Phi\Phi}}, \qquad \tilde{\eta} = \eta \left(S_{JJ}/S_{\Phi\Phi}\right)^{1/4}, \tag{3.44}$$

and summing equation (3.40) and equation (3.43) into the total measurement noise

$$S_{zz}^{\text{meas}}(\omega) = S_{\Phi\Phi}\eta^{-2} + |\chi(\omega)|^2 \eta^2 S_{JJ} = \kappa \left(\tilde{\eta}^{-2} + \tilde{\eta}^2 |\chi(\omega)|^2\right). \tag{3.45}$$

The parameter κ is called the energy resolution of the SQUID and it is derived from the time-energy uncertainty principle of quantum mechanics. Because of the there is a lower limit of $\kappa = \hbar$ that defines the so called *Standard Quantum Limit* or SQL. While the SQL is theoretically possible, current SQUIDs are mostly optimized to achieve energy resolution near the order of $50h$, h being Plank's constant [34]. SQUIDs used in Chalmers offer $\kappa = 45h$, which is the value we are going to use for calculations later.

The choice of η parameter is a bit more tricky. As mentioned before, the value η has different effects on the imprecision and back-reaction noise. The optimal choice resides on the specific frequency one wants to measure. In this thesis we are going to use the limit of $\tilde{\eta}$

$$\tilde{\eta} = \sqrt{m_l}\, \omega_l \tag{3.46}$$

called the *broadband limit*, which is the same as the simplest case in [28]. Without delving too much into the specifics, this is the best choice for η if one wants to have the lowest measurement noise for the widest range of frequencies. The only drawback is that the broadband limit induces greater noise in the interval near the resonance frequency f_l. Practically speaking, the variation of η in a future experimental setup can be achieved by coupling to the SQUID a microwave resonator that performs a dispersive readout and by increasing, or decreasing, the number of photons in the resonator.

4
Results

In this chapter we are going to present the computational results for the motion of the levitated superconductor. Based on simulations and considering all of the possible noise sources (vibrations, thermal, imprecision, back-action) we are going to give some estimates on the sensitivity of a levitated experiment with realistic parameters and in a case of severely reduce vibrational noise.

4.1 Two-stage model results

In this section we will present the computational results for the two-stage vibration isolation system.

4.1.1 Vibrational noise floor

To get a first idea of the vibrational noise power spectral density magnitude, we test our computational model for zero dark matter signal and zero noise from other sources. The trajectory $z(t)$ is computed by solving the differential equations (3.11) and (3.10) using the `solver.ivp` method[1] in Python.

Table 4.1: System Parameters of a proposed levitated experiment.

Quantity	**Value**
Target mass m_l [kg]	7×10^{-10}
Trap frequency $\omega_l/2\pi$ [Hz]	100
Trap damping γ_l [Hz]	10^{-6}
Platform mass m_p [kg]	2.0
Platform frequency $\omega_p/2\pi$ [Hz]	1.0
Platform damping γ_p [Hz]	0.1

The process was repeated in a Monte Carlo loop for different realizations of y(t), as described in section 3.2.1, where the vibration PSD of $y(t)$, being the coordinate of the base connected to earth, was given by equation (3.14), plotted in figure 4.1. Note

[1]The `solver.ivp` can be used with several internal methods (see [35] for more). At first the default `RK45` was used, but the resulting PSD and mean trajectory exhibited several numerical artifacts, probably due to the high quality factor of the system. After some trials the `BDF` method was chosen for every calculation, since it gave the most accurate results, albeit being computationally intensive.

that the S_{yy} used is a linear approximation of the actual seismic noise measured in the MC2 lab environment as seen in [36]. Low frequency noise is assumed to be flat for further simplification. After 100 realizations, the mean and standard deviation of $z(t)$ are taken (figure 4.2). The time span of the simulations was $t = 60$ s, where the first 10 seconds were culled to have a better initial condition approximation. The values of experimental parameters used for this and every other simulation are shown in table (4.1).

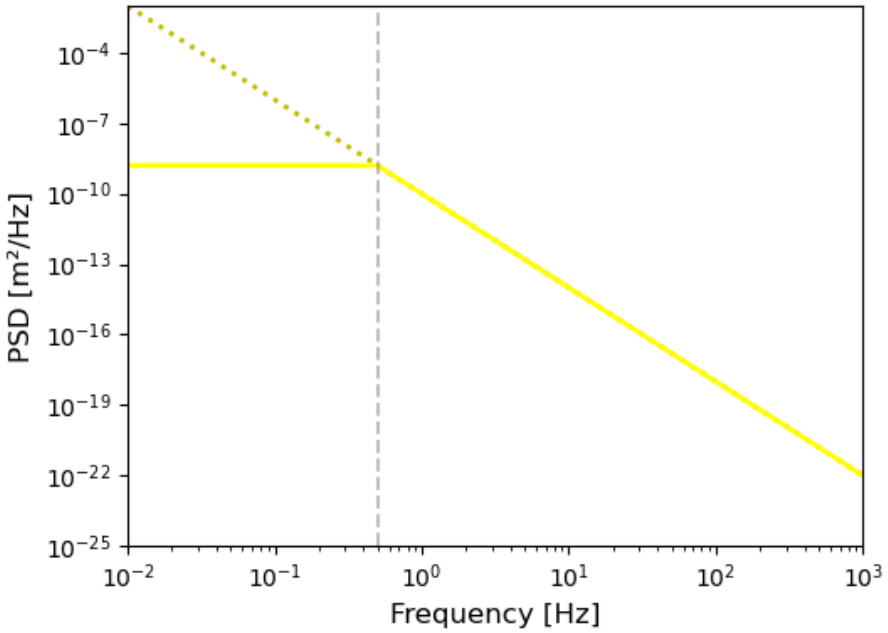

Figure 4.1: PSD for the vibrational noise, stemming from the motion of the base with coordinate $y(t)$. The yellow dotted line is a rough approximation of the MC2 lab measured noise, taken from [36]. The solid line is another approximation, where noise is flattened for frequencies lower than 0.5 Hz, which is the PSD used in simulations.

4.1.2 Effective temperature

Looking at figure (4.2) we can already make some rough estimations about the effective temperature. The mean square displacement amplitude appears to be $\langle z^2 \rangle \sim (5 \times 10^{-5})^2 = 2.5 \times 10^{-9}$ m^2. If we consider that after the culling time of 10 seconds the system is in an approximate thermal equilibrium, then from the equipartition theorem (equation (3.21)), we estimate that the environmental temperature of $T_{\text{env}} = 20$ mK would cause mean square displacement amplitude of $\langle z^2 \rangle_{\text{env}} \approx 10^{-21}$ m^2. Thus, we can already see that the external vibrations thermalize the levitated superconductor several orders of magnitude more than the ultra cold environment of the experiment.

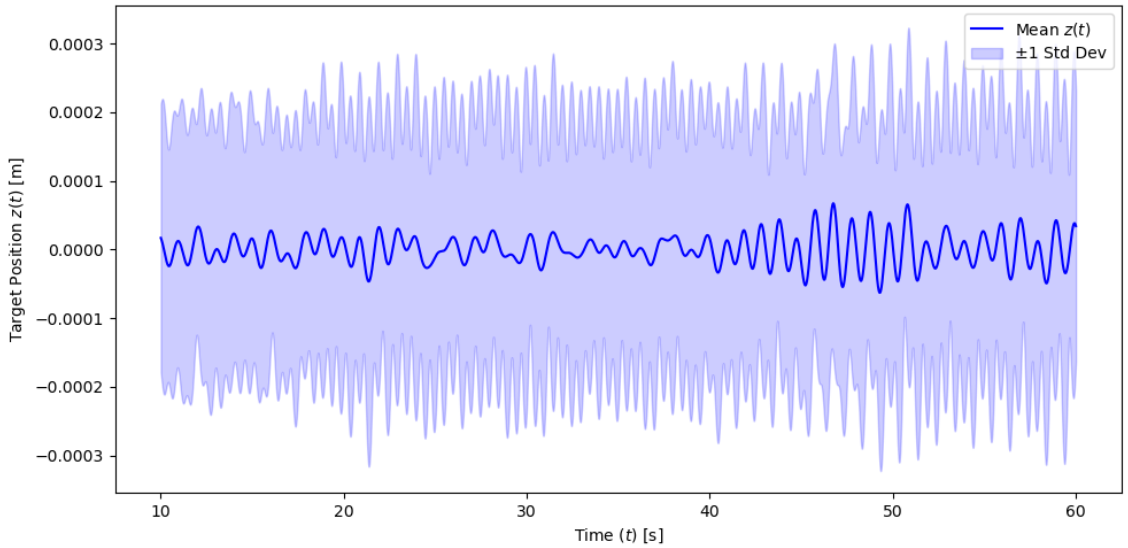

Figure 4.2: Trajectory of the levitated object, where vibrational noise is the only noise source and DM signal is turned off. Blue curve represents the mean $z(t)$ after 100 Monte Carlo simulations, light blue interval is the ± 1 standard deviation.

We can also confirm this by numerical computation of the integral in equation (3.38), which was derived analytically. Similarly to the simulations, the $\omega/2\pi < 0.5$ Hz area of the integrand assumes flat S_{yy}. Since the integrand exhibits prominent resonance effects we will also make some numerical approximations for its value, being $\langle z^2 \rangle \approx 1.13 \times 10^{-8}$ m^2
This aligns well with what we observe from the simulations. We conclude that the vibrational noise dominates the thermal noise in this model. As we will see later the vibrational noise dominates the lower frequency regime all together even over the quantum measurement noise.

4.1.3 Power spectral densities

The primary output of interest is the power spectral density (PSD) of the target oscillator's displacement, $S_{zz}(f)$. This quantifies the power distribution of the displacement signal over frequency.

For each realization of the culled $z(t)$, its PSD is estimated using *Welch's method*[2], implemented via `scipy.signal.welch`. The time series $z(t)$ is divided into (potentially overlapping) segments of length N_{perseg}. Each segment is multiplied by a windowing function, chosen to be the `Hann` window function, to reduce spectral leakage. The Fourier transform is then computed for each segment and the square magnitude is taken to obtain its periodoram. The periodograms from all segments are averaged, to reduce the variance of the estimate. The degree of overlap between segments (typically $N_{\text{perseg}}/2$) influences the trade-off between variance reduction

[2]An alternative to this method, called the *average periodogram* was also tested, but was not chosen because it was too computationally intensive.

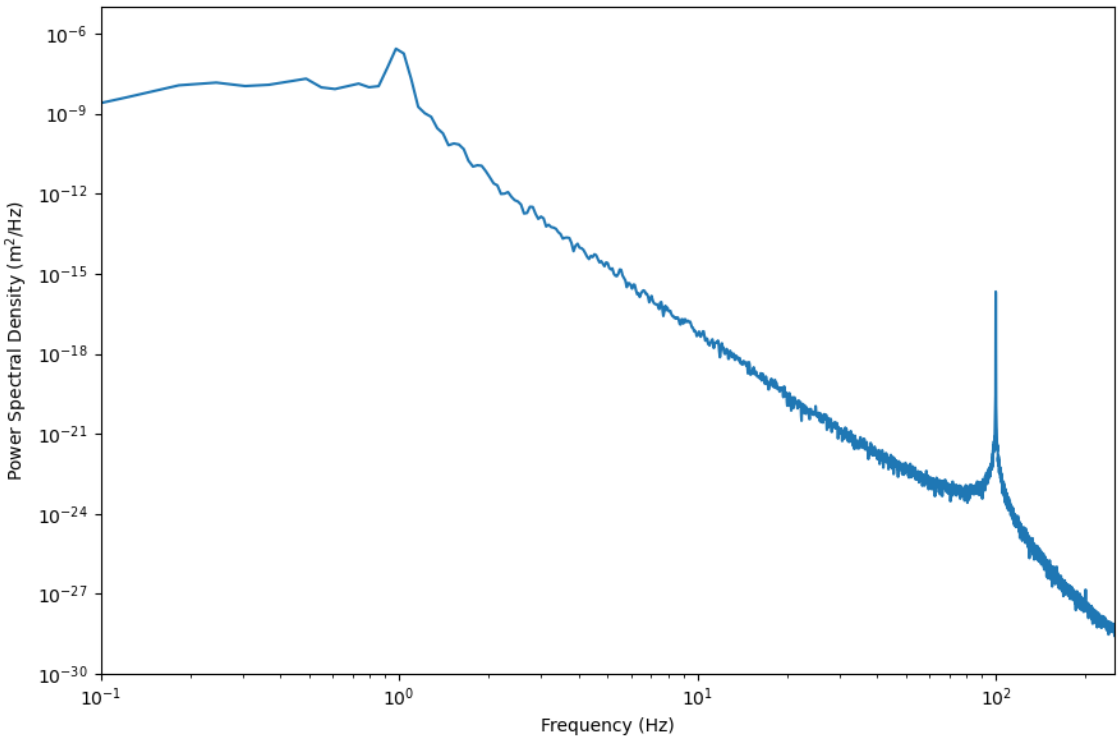

Figure 4.3: PSD $S_{zz}^{\text{vib}}(\omega)$ for 100 Monte Carlo simulations, representing the vibrational noise floor, for $\delta = 10^{-10}$ m^2 Hz^2.

.

and frequency resolution. In our computations, the frequency domain has a maximum of 500 Hz (meaning 25000 evaluation points for an integration time of $t_{int} = 50$ s), thus a frequency resolution $\Delta f = 500/N_{\text{perseg}}$. The $N_{\textbf{perseg}}$ was chosen to be $N_{\text{perseg}} = 8192$ so we could have a good frequency resolution of $\Delta f = 0.061$ Hz, which would be essential for computing the very sharp peaks of the DM signal. The result of this method is a PSD estimate for the n-th realization at a common set of frequencies. The final PSD is obtained by averaging the PSDs from all successful Monte Carlo realizations.

Example of such a PSD is the S_{zz}^{vib}, plotted in figure 4.3, in which the DM signal is turned of in order to have just the vibrational noise floor. The rest of the PSDs can be plotted (figure 4.4) by just using the analytical formulas of equation (3.40) and equation (3.43) and the broadband limit of equation (3.46).

4.2 Signal-to-noise ratio analysis

Having PSDs for every noise source, we can finally add a DM signal to the system and see the results. What we will do is essentially a repetition of the methods described in section 4.1.3, but this time the DM force in equations (3.10) and (3.11) would be non-zero. The expected result would be a similar PSD but with a visible peak in the frequency of the DM signal, provided the coupling is sufficient.

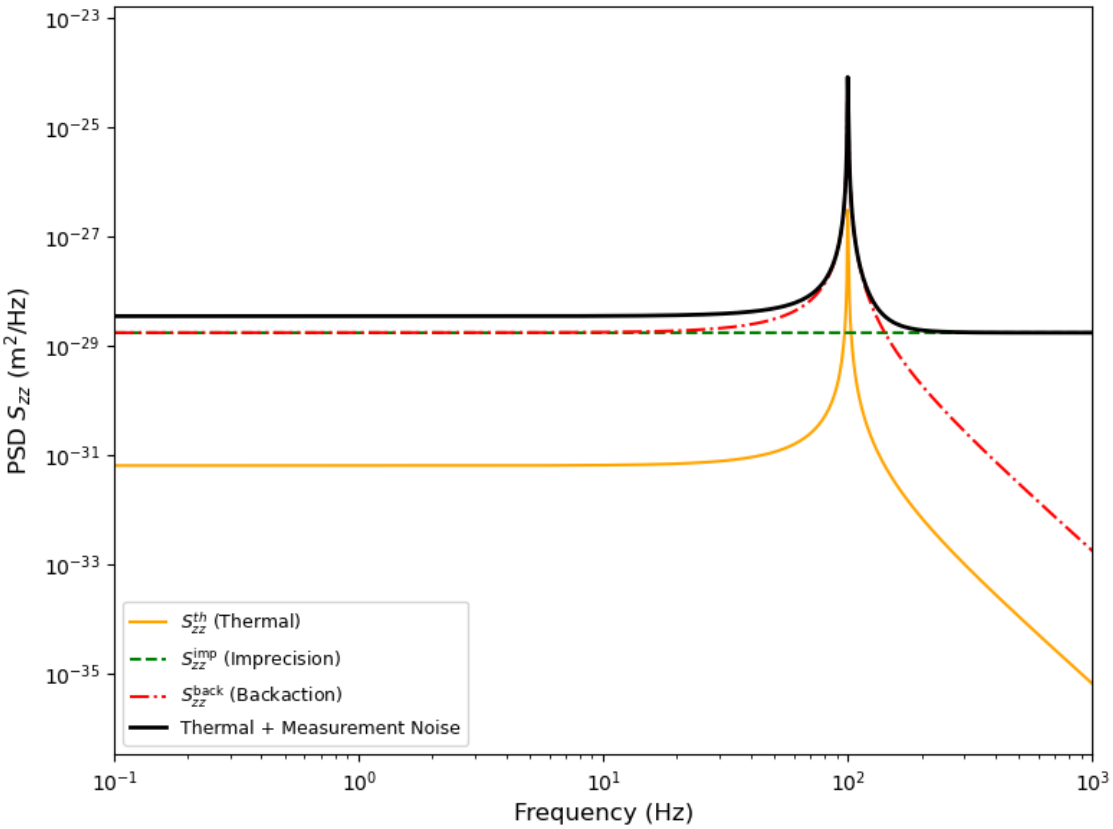

Figure 4.4: Position power spectral densities for thermal noise (orange), imprecision noise (dashed green) and back-reaction (dashed red), where $\tilde{\eta}$ is chosen to be on the broadband limit and $\kappa = 45h$.

The signal is a displacement amplitude, whose source is the DM induced force of equation (3.13), where parameters are taken from table 4.1. The neutron number is estimated to be $N_p = 6.25 \times 10^{26}$ for the aluminum platform and $N_l = 3.64 \times 10^{16}$ for the superconducting sphere made out of lead (as discussed in section 3.1 the sphere must be made from a type-I superconductor, with alternative materials being Al, In, etc.). Then the force in the form of

$$F_{\mathrm{l,p}}^{DM} = N_{\mathrm{l,p}} y_{\phi n} F_0 \sin(\omega\, t) \tag{4.1}$$

will have amplitude $F_0 = 2.014 \times 10^{-18}$ kg m/s, for $\rho_{\mathrm{DM}} = 0.4$ GeV^2 [37] and $v = 10^{-3}c$.

Thus, the next step would be to properly determine the magnitude of the minimum required coupling that can be "seen" in the resulting displacement PSD. This will be done with a `Signal-to-noise ratio` analysis. With this we can estimate through simulations the minimum required coupling for a set range of signal frequencies. The minimum DM signal frequency we will test would be 20 Hz, as a lower frequency range would be affected too much from the vibrational noise. The maximum DM frequency we will test would be 500 Hz. Higher test frequencies (up to 1 kHz) could be realistically detected by the experiment, but in our simulation model the higher

frequencies require a bigger N_{perseg} to maintain a good frequency resolution in that interval, which would make the model too computationally intensive for the purpose for getting a sensitivity estimation. Our testing frequency interval corresponds to masses from 8.27×10^{-14} eV to 2.06×10^{-12} eV.

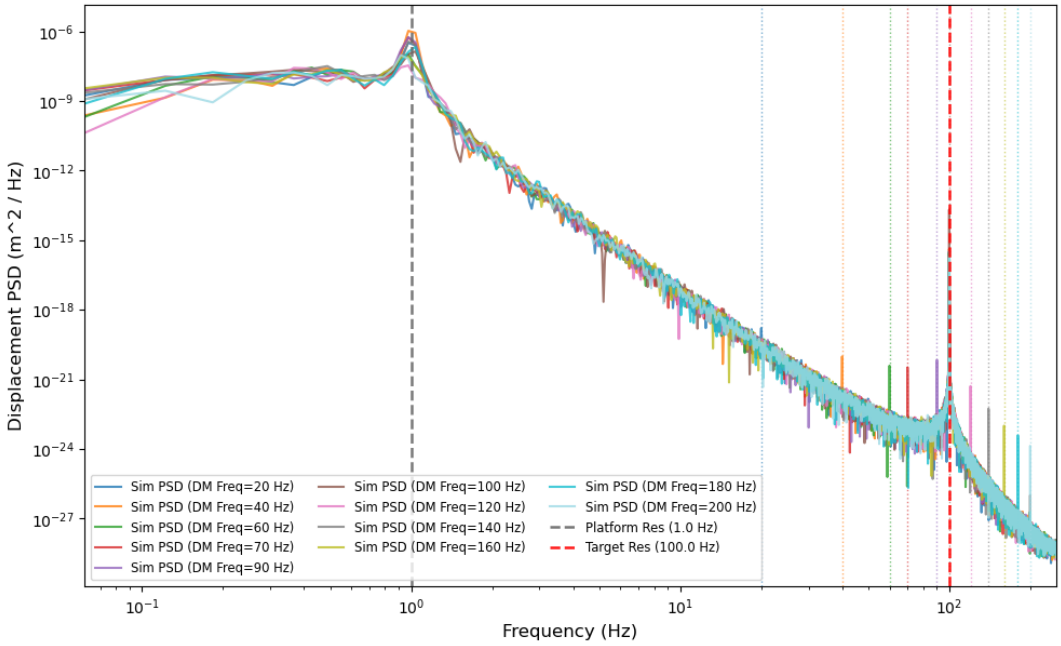

Figure 4.5: PSD of a frequency scan (11 frequencies) for fixed coupling $y_{\phi n} = 5 \times 10^{-17}$, where noise from external vibrations, thermal environment (T=20mK) and quantum measurement is included (broadband limit).

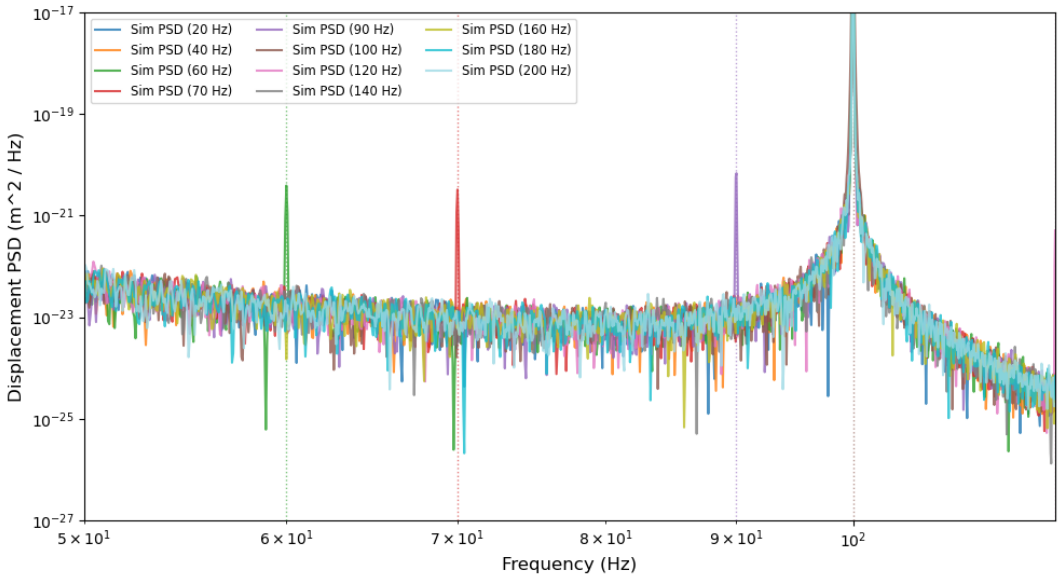

Figure 4.6: Zoomed in version of the PSD of figure 4.5. Three sharp frequency peaks are observed exactly at the DM signal frequencies of 60, 70, 90 Hz.

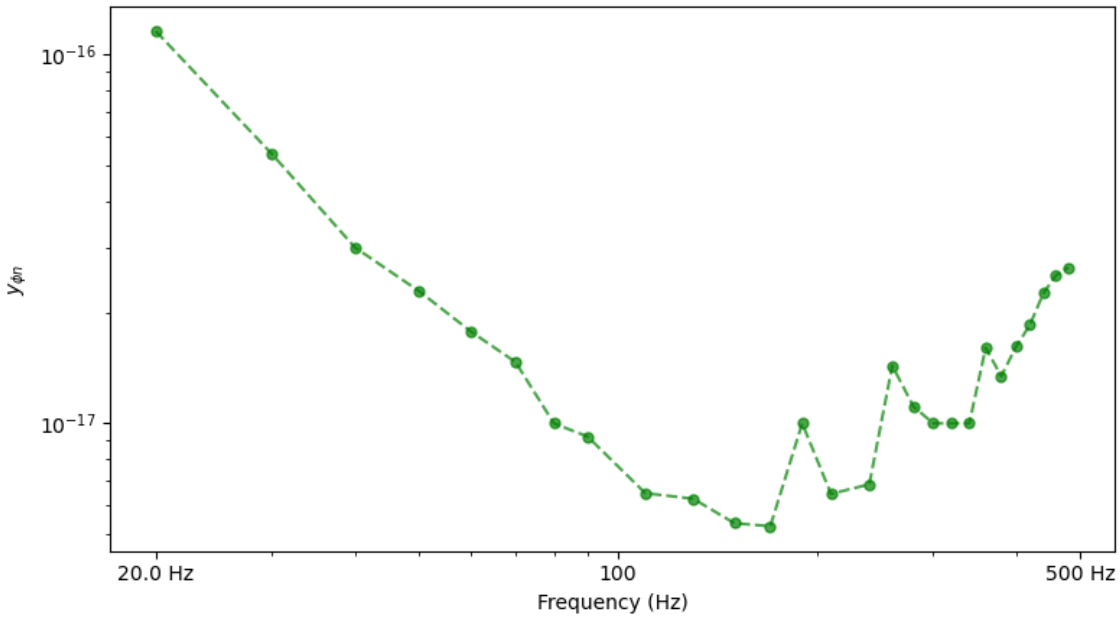

Figure 4.7: Sensitivity estimate for $\delta = 10^{-10}$ m^{2}Hz^3. Points are simulation results for each individual DM frequency probed. Resonance frequency $f_l = 100$ Hz is excluded since we are working on the broadband limit.

4.2.1 Two-stage model simulations

The simulations give a total PSD with the DM signal included. For visualization, see the frequency scans plotted in figure 4.5 and figure 4.6, where the scanning DM signal has a fixed coupling of $y_{\phi n} = 5 \times 10^{-17}$. PSDs like these were calculated for a wider frequency interval (20-500 Hz, with 10 Hz increment until the resonance frequency, and 20 Hz increment after) albeit for 20 Monte Carlo simulations each. The SNR then is just the ratio of the signal peak and the noise floor in the PSD. For this, a threshold of SNR=3 was chosen, same as in [28], to find the minimum required coupling that could reach it. Computationally this was done by a bisection search on a preset range of couplings. After each bisection calculation the range was updated based on wether the calculated SNR is above or below the threshold. When the calculated SNR reaches (approximately) the threshold, the process repeats for the next signal frequency.

The result is a sensitivity estimation based on the minimum coupling simulation, as shown in figure 4.7.

4.2.2 Scaled down δ

It is apparent by now that the two-stage model offers vibrational shielding that can be improved. This can be done by adding more stages to the system, thus having more differential equations. With our current method for estimating sensitivity this would increase computational times dramatically. Thus we are going to consider an approximation to deal with vibrational noise, which may be the simplest one: we

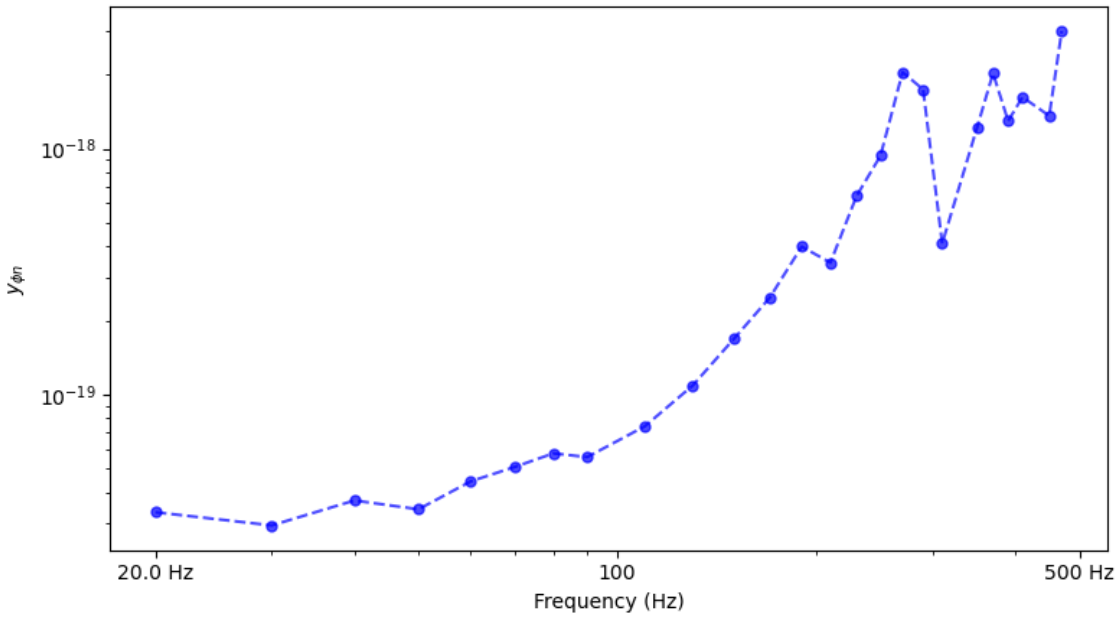

Figure 4.8: Sensitivity estimate for $\delta' = 10^{-20}$ m^{2}Hz^3. Points are simulation results for each individual DM frequency probed. Resonance frequency $f_l = 100$ Hz is excluded since we are working on the broadband limit.

are going to assume that a system connected to the platform linearly reduces the δ parameter, i.e. the new delta would be

$$\delta' = \epsilon\delta \tag{4.2}$$

where $\epsilon \ll 1$. While efficient, this approach is not the most rigorous. For once, the vibrational noise that is fed into the system is frequency dependent (at least above a certain frequency) i.e. we have a colored noise model. Better vibrational shielding is generally designed to filter certain frequencies of this colored noise and not reduce linearly the whole spectrum. Our approach may be more suited for a white noise model, where there is no frequency dependence, but it should be sufficient as a measure of comparison with our crude two-stage model.

Since we are theoretically reducing the vibrational noise to a great extend, we can use the results of section 4.1.2 to estimate the ϵ parameter. For the vibrational noise to dip near the order of the thermal noise we should need a reduction of $\mathcal{O}(-12)$ in the square displacement amplitude, thus a reduction of 1 to 1,000,000 in the noise amplitude. We know however, that the measurement noise exceeds the thermal noise by $\mathcal{O}(2)$ from figure 4.4, thus the theoretical reduction of the vibrational noise to the thermal level may not be fruitful. This motivates us to choose $\epsilon = 10^{-10}$, thus having a 1 to 100,000 reduction in noise amplitude. We repeat the simulations for the new, scaled down delta and plot the results in figure 4.8.

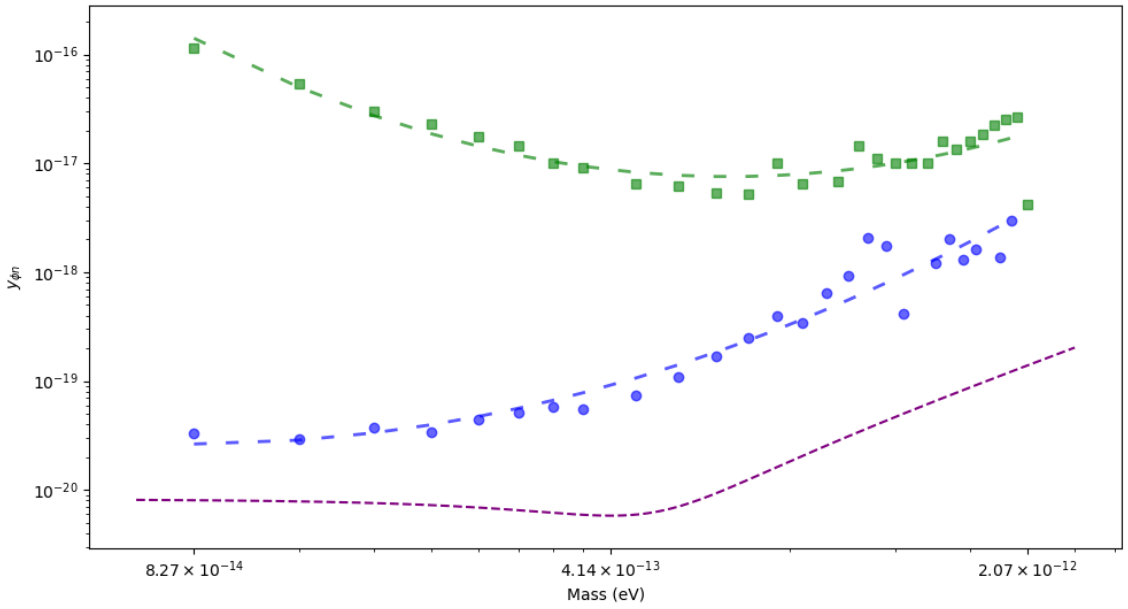

Figure 4.9: Combined plot of sensitivity estimates. Green dashed line is a curve fit to the data of figure 4.7, while blue dashed line is a fit to the data of figure 4.8. Purple dashed line is the projection without vibrational noise, according to equation (4.3).

4.2.3 Analytical SNR

Projections for sensitivity can be also done with an analytical expression of the SNR. This would help us compare an ideal case with our simulation model. For small observation times, the SNR is given by

$$\mathrm{SNR} = \frac{|Z_{DM}|^2 \, T_{\mathrm{obs}}}{2 S_{zz}^{\mathrm{tot}}}, \tag{4.3}$$

where S_{zz}^{tot} is the total noise, taken to be the thermal (equation (3.19)) and measurement noise (equation (3.43) and the signal displacement amplitude $|Z_{DM}|$ is given by

$$|Z_{DM}| = y_{\phi n} \, |\chi(\omega)| \, \frac{N_l F_0}{m_l} \tag{4.4}$$

As before we set SNR=3, η parameter according to equation (3.46) and $\kappa = 45h$. Usually in literature the vibrational noise is neglected e.g. assuming the use of a wide array of experiments and not a single sensor, the vibrational background could theoretically be eliminated with statistics [31]. Thus having an estimation neglecting the vibrational noise can be useful to set some ideal boundary for complete mitigation of that source (see figure 4.9).

5

Conclusion

The product of our analysis is the estimate on the coupling constraints a future magnetic levitation experiment can put on the area of $10^{-14} - 10^{-12}$ eV, which is shown on figure 4.9.

The first experiment of this kind [29] have put a constrain on $g_{B-L} \leq 2.98 \times 10^{-21}$, which can be rescaled according to equation (1.5) to our scalar coupling $y_{\phi n} \leq 2.98 \times 10^{-18}$, for a mass range of $1.1036 - 1.1048 \times 10^{-13}$ eV. This falls between the two-stage model and "ideal isolation" model estimates, giving us a confirmation that with a better vibration isolation the estimates of figure 4.9 can be realistically achieved. Specifically the experiment in [29] uses a 2+7 stage system, effectively achieving vibration isolation of 80 dB, meaning a reduction of the noise amplitude by a 10^{-4} factor. For comparison our theoretical "ideal isolation" reduced the amplitude by more than 10^{-5} before taking into account the two-stage isolation. Another difference is that our model takes into account the broadband limit regarding the measurement noise, and in general assumes that the detection strategy would be frequency scans over a sizable mass range (i.e. frequency of 20-500 Hz), while the experiment done was mainly a resonant frequency test at around $f_l = 26.7$ Hz.

Furthermore, the estimates of figure 4.9 do not take into account any statistical analysis. For example, on the matter of scalar WDM a statistical analysis considering only thermal fluctuations was done in [38] with the Asimov dataset method. While we do not expect our numerical simulation estimates to deviate much after such an analysis, it's inclusion would be an essential complementary study to our model.

On the matter of the direction of the force, we assumed in our one-dimensional model that the total bulk of the force comes from a single preferred direction, which aligns with the coordinates x, y, z used for the simulations. Other studies ([28] , [26]) assume that the direction is entirely random, and the velocities are distributed uniformly in the three dimensional space. This can be mitigated in our model by rescaling the average DM density ρ_{DM} to be $\sqrt{\frac{2\rho_{DM}}{3}}$ in the force amplitude of equation 4.1, essentially adding a $1/\sqrt{3}$ factor to the coupling and/or considering a three dimensional model. One can also consider a specific preferred direction based on the standard dark matter halo model [39], i.e. by modeling the direction of the DM signal based on the position of the earth on the galactic frame.

Another aspect not considered in the thesis is the coherence time. In our theory and computational model we considered the approximation $\omega_\phi \approx m_\phi$, implying that the

investigated wave of dark matter is a result of a superposition of an extremely large number of individual dark matter waves, with the total having a uniform frequency with an extremely small frequency spread of $\delta\omega_\phi \sim v/\lambda = v^2 m_\phi$, which leads to the sharp peaks observed in figure 4.6. This frequency spread defines a relatively large coherence time $T_{coh} \sim 10^6/\omega_\phi$. Thus our model works for $T_{\mathrm{obs}} < T_{\mathrm{coh}}$, which is frequency depended. For our simulations the same integration time of $T_{\mathrm{obs}} = 1$ min was taken, but since the coherence time differs with frequency (dropping to $\sim$ 16 min for the 1kHz frequency) the integration time can be further optimized, essentially leading to better sensitivity estimates according to equation 4.3.

In conclusion, taking into account every approximation and simplification made, this thesis shows through numerical simulations that with current technological capabilities a good sensitivity regarding scalar wave dark matter can be achieved.

Bibliography

[1] F. Zwicky. Die Rotverschiebung von extragalaktischen Nebeln. *Helv. Phys. Acta*, 6:110–127, 1933.

[2] F. Mandl and G. Shaw. *Quantum Field Theory*. A Wiley-Interscience publication. Wiley, 2010.

[3] J.J. Sakurai and J. Napolitano. *Modern Quantum Mechanics*. Cambridge University Press, 2020.

[4] Lam Hui. Wave dark matter. *Annual Review of Astronomy and Astrophysics*, 59(1):247–289, September 2021.

[5] David J.E. Marsh. Axion cosmology. *Physics Reports*, 643:1–79, July 2016.

[6] Michael E. Peskin and Daniel V. Schroeder. *An Introduction to Quantum Field Theory*. Westview Press, Boulder, CO, 1995.

[7] Virginia Trimble. Existence and nature of dark matter in the universe. , 25:425–472, January 1987.

[8] Sinclair Smith. The Mass of the Virgo Cluster. , 83:23, January 1936.

[9] M. Persic, P. Salucci, and F. Stel. The universal rotation curve of spiral galaxies: I. the dark matter connection. *Monthly Notices of the Royal Astronomical Society*, 281(1):27–47, 1996.

[10] V. C. Rubin, W. K. Ford, Jr., and N. Thonnard. Extended rotation curves of high-luminosity spiral galaxies. IV. Systematic dynamical properties, Sa -> Sc. , 225:L107–L111, November 1978.

[11] A. Bosma. 21-cm line studies of spiral galaxies. I. Observations of the galaxies NGC 5033, 3198, 5055, 2841, and 7331. , 86:1791–1824, December 1981.

[12] Katherine Garrett and Gintaras Duda. Dark matter: A primer. *Advances in Astronomy*, 2011:1–22, 2011.

[13] D. Walsh, R. F. Carswell, and R. J. Weymann. 0957+561 A, B: twin quasistellar objects or gravitational lens? , 279:381–384, May 1979.

[14] R. Lynds and V. Petrosian. Giant Luminous Arcs in Clusters of Galaxies. In J. Audouze, M. C. Pelletan, A. Szalay, Ya. B. Zel'dovich, and P. J. E. Peebles, editors, *Large Scale Structures of the Universe*, volume 130 of *IAU Symposium*, page 467, January 1988.

[15] A. G. Bergmann, V. Petrosian, and R. Lynds. Gravitational lens models of arcs in clusters. *Astrophysical Journal*, 350:23–35, February 1990. ISSN 0004-637X.

[16] Gianfranco Bertone, Dan Hooper, and Joseph Silk. Particle dark matter: evidence, candidates and constraints. *Physics Reports*, 405(5–6):279–390, January 2005.

[17] Tisserand, P., Le Guillou, L., Afonso, C., Albert, J. N., Andersen, J., Ansari, R., Aubourg, É., Bareyre, P., Beaulieu, J. P., Charlot, X., Coutures, C., Ferlet,

R., Fouqué, P., Glicenstein, J. F., Goldman, B., Gould, A., Graff, D., Gros, M., Haissinski, J., Hamadache, C., de Kat, J., Lasserre, T., Lesquoy, É., Loup, C., Magneville, C., Marquette, J. B., Maurice, É., Maury, A., Milsztajn, A., Moniez, M., Palanque-Delabrouille, N., Perdereau, O., Rahal, Y. R., Rich, J., Spiro, M., Vidal-Madjar, A., Vigroux, L., and S. Zylberajch (The EROS-2 collaboration). Limits on the macho content of the galactic halo from the eros-2 survey of the magellanic clouds ***. *AA*, 469(2):387–404, 2007.

[18] Adrian Cho and Richard Stone. Racing to capture darkness. *Science*, 317(5834):32–34, 2007.

[19] J. Bovy and S. Tremaine. On the local dark matter density. *The Astrophysical Journal*, 756(1):89, 2012.

[20] C. F. McKee, A. Parravano, and D. J. Hollenbach. Stars, gas, and dark matter in the solar neighborhood. *The Astrophysical Journal*, 814(1):13, 2015.

[21] Wayne Hu, Rennan Barkana, and Andrei Gruzinov. Fuzzy cold dark matter: The wave properties of ultralight particles. *Phys. Rev. Lett.*, 85(6):1158–1161, 2000.

[22] Steven Weinberg. A new light boson? *Phys. Rev. Lett.*, 40:223–226, Jan 1978.

[23] Roberto D. Peccei. *The Strong CP Problem and Axions*, page 3–17. Springer Berlin Heidelberg, 2008.

[24] P. Di Vecchia and G. Veneziano. Chiral dynamics in the large n limit. *Nuclear Physics B*, 171:253–272, 1980.

[25] Bob Holdom. Two u(1)'s and charge shifts. *Physics Letters B*, 166(2):196–198, 1986.

[26] Peter W. Graham, David E. Kaplan, Jeremy Mardon, Surjeet Rajendran, and William A. Terrano. Dark matter direct detection with accelerometers. *Physical Review D*, 93(7), 2016.

[27] J. Hofer, R. Gross, G. Higgins, H. Huebl, O. F. Kieler, R. Kleiner, et al. High-q magnetic levitation and control of superconducting microspheres at millikelvin temperatures. *Phys. Rev. Lett.*, 131:043603, 2023.

[28] G. Higgins, S. Kalia, and Z. Liu. Maglev for dark matter: Dark-photon and axion dark matter sensing with levitated superconductors. *Phys. Rev. D*, 108(1):012003, 2023.

[29] Dorian W. P. Amaral, Dennis G. Uitenbroek, Tjerk H. Oosterkamp, and Christopher D. Tunnell. First search for ultralight dark matter using a magnetically levitated particle, 2024.

[30] Wieczorek Lab. Quantum technologies and foundations with hybrid nano- and micromechanical systems. `https://wieczorek-lab.com/`.

[31] Daniel Carney, Anson Hook, Zhen Liu, Jacob M Taylor, and Yue Zhao. Ultralight dark matter detection with mechanical quantum sensors. *New Journal of Physics*, 23(2):023041, February 2021.

[32] Måns Anduri. Searching for vector wave dark matter with levitated magnetomechanics: Analysis of a hypothetical direct detection experiment using levitating superconductive test objects. Master's thesis, Chalmers University of Technology, Gothenburg, Sweden, 2023.

[33] M. Tinkham. *Introduction to Superconductivity*. McGraw-Hill, 2nd edition, 1996.

[34] D. Drung, C. Abmann, J. Beyer, A. Kirste, M. Peters, F. Ruede, and Th. Schurig. Highly sensitive and easy-to-use squid sensors. *IEEE Transactions on Applied Superconductivity*, 17(2):699–704, 2007.

[35] Pauli Virtanen, Ralf Gommers, Travis E Oliphant, Matt Haberland, Tyler Reddy, David Cournapeau, Evgeni Burovski, Pearu Peterson, Warren Weckesser, Jonathan Bright, et al. Scipy 1.0: fundamental algorithms for scientific computing in python. *Nature Methods*, 17(3):261–272, 2020.

[36] Anton Söderqvist. Cryogenic vibration isolation for low frequency levitation experiments. Master's thesis, University of Glasgow and Chalmers, 2023.

[37] Riccardo Catena and Piero Ullio. A novel determination of the local dark matter density. *Journal of Cosmology and Astroparticle Physics*, 2010(08):004–004, August 2010.

[38] Amanda Carlsson Salomon. Searching for scalar wave dark matter with levitated magnetomechanics: Sensitivity studies for a hypothetical direct detection experiment using superconducting levitating objects. Master's thesis, Chalmers University of Technology, Gothenburg, Sweden, 2023.

[39] Joshua W. Foster, Nicholas L. Rodd, and Benjamin R. Safdi. Revealing the dark matter halo with axion direct detection. *Phys. Rev. D*, 97:123006, Jun 2018.

A

Quantum Fluctuations

A free real scalar quantum field $\phi(x)$ can be expanded in terms of creation ($a_k^\dagger$) and annihilation (a_k) operators:

$$\phi(x) = \int \frac{d^3k}{(2\pi)^3\sqrt{2\omega_k}} \left[a_k e^{-ik\cdot x} + a_k^\dagger e^{ik\cdot x}\right], \tag{A.1}$$

where $\omega_k = \sqrt{k^2 + m^2}$ is the energy for a particle of mass m and momentum k. The operators satisfy the bosonic commutation relations:

$$[a_k, a_{k'}^\dagger] = \delta^3(k - k'), \quad [a_k, a_{k'}] = 0, \quad [a_k^\dagger, a_{k'}^\dagger] = 0. \tag{A.2}$$

The number operator for a specific mode k is given by

$$N_k = a_k^\dagger a_k. \tag{A.3}$$

The free Hamiltonian of the field is the superposition of single mode Hamiltonians:

$$H = \sum_k \left(N_k + \frac{1}{2}\right) \tag{A.4}$$

A single mode state $|c\rangle$, i.e. a state of just one momentum $\vec{k}$, is a *coherent state* if it is also an eigenstate of a single mode Hamiltonian:

$$a_k|c\rangle = c|c\rangle, \tag{A.5}$$

where $c = |c|e^{-i\delta}$ is any complex number of modulus $|c|$ and phase δ. The expectation value of N_k is

$$\langle N_k\rangle = \langle c|N_k|c\rangle = |c|^2. \tag{A.6}$$

For the expectation value of N_k^2:

$$\langle N_k^2\rangle = \langle c|a_k^\dagger a_k a_k^\dagger a_k|c\rangle \tag{A.7}$$

$$= \langle c|a_k^\dagger(a_k^\dagger a_k + 1)a_k|c\rangle \tag{A.8}$$

$$= \langle c|(a_k^\dagger a_k a_k^\dagger a_k + a_k^\dagger a_k)|c\rangle \tag{A.9}$$

$$= |c|^4 + |c|^2. \tag{A.10}$$

Thus, the variance is

$$(\Delta N_k)^2 = \langle N_k^2\rangle - \langle N_k\rangle^2 = |c|^2 = \langle N_k\rangle. \tag{A.11}$$

The relative fluctuation, which in our case represents the quantum fluctuations of the particle number, is

$$\frac{\Delta N_k}{\langle N_k\rangle} = \frac{\sqrt{\langle N_k\rangle}}{\langle N_k\rangle} = \langle N_k\rangle^{-1/2}. \tag{A.12}$$

DEPARTMENT OF PHYSICS
CHALMERS UNIVERSITY OF TECHNOLOGY
Gothenburg, Sweden
www.chalmers.se

CHALMERS
UNIVERSITY OF TECHNOLOGY